Theoretical study of collective modes in DNA at ambient temperature

Simona Cocco[a)]
Dipartimento di Scienze Biochimiche, Università di Roma ''La Sapienza,'' P.le A. Moro, 5 - 00185 Roma, Italy, and CNRS-Laboratoire de Physique de l'ENS-Lyon, 46 Allée d'Italie, 69364 Lyon Cedex 07, France, and CNRS-Laboratoire de Physique Théorique de l'ENS, 24 rue Lhomond, 75005 Paris, France

Rémi Monasson[b)]
CNRS-Laboratoire de Physique Théorique de l'ENS, 24 rue Lhomond, 75005 Paris, France

(Received 10 November 1999; accepted 15 March 2000)

The instantaneous normal modes corresponding to radial hydrogen bonds vibrations, torsion, and axial compression fluctuations of a DNA molecule model at ambient temperature are theoretically investigated. Due to thermal disorder, normal modes are not plane waves with a single wave number q but have a finite and frequency dependent damping width. The density of modes $\rho(\nu)$, the average dispersion relation $\nu(q)$, as well as the coherence length $\xi(\nu)$ are analytically calculated. The Gibbs averaged resolvent is computed using a replicated transfer matrix formalism and variational wave functions for the ground and first excited state. Our results for the density of modes are compared to Raman spectroscopy measurements of the collective modes for DNA in solution and show a good agreement with experimental data in the low frequency regime $\nu<150$ cm^{-1}. Radial optical modes extend over frequencies ranging from 50 to 100 cm^{-1}. Torsional and compressional acoustic modes are limited to $\nu<25$ cm^{-1}. Normal modes are highly disordered and coherent over a few base pairs only ($\xi<15$ Å) in good agreement with neutron scattering experiments. © *2000 American Institute of Physics.* [S0021-9606(00)50622-9]

I. INTRODUCTION

Much attention has been paid in the last 20 years to low frequency dynamics of DNA due to its relevance to biological processes. Vibrational modes involving collective motions of groups of atoms have been investigated by means of various techniques as neutron scattering,[1–3] numerical simulations,[4] spectroscopy measurements, NMR, etc.[5–10] Among the latter, Raman studies carried out by H. Urabe *et al.*[7–9,11] have revealed particulary useful to gain information on the dependence of low frequency vibrations properties of DNA upon external conditions, e.g., water content, ionic concentration, temperature. The observation of the Raman scattering intensity in the low frequency region is technically very difficult because the strong solvent Rayleigh scattering near zero frequency masks the DNA response. Nevertheless a broad band ranging from 50 to 100 cm^{-1} has been evidenced and associated to hydrogen-bonded base pair vibrations.[7,8] Moreover experiments focusing on oriented solid DNA fibers have also exhibited sharp peaks in the Raman intensity at $\simeq 16$ cm^{-1}, that shifts toward lower frequency region when raising the degree of hydration.[9] The origin of this peak, in particular, its interhelical, or intrahelical nature has been debated for a long time.[11]

To reach a better understanding of the above experimental findings, detailed theoretical analysis of DNA vibrational motions have been proposed. Devoting particular attention to hydrogen bond stretching modes, Prohofsky and collaborators[12] have been able to find a vibration mode at 85 cm^{-1} and confirm its origin. Their approach is based on a detailed description of the DNA molecule at the atomic level[13] and a variational calculation method, called modified self-consistent phonon approximation (MSPA). Within MSPA, the molecule at ambient temperature is reduced to an effective (and complex) harmonic lattice, the force constants of which are determined in a self-consistent way. This approach has been very useful in calculating many properties of DNA, e.g., the melting of DNAs of different sequences,[14,15] the temperature and salt dependence of the *B* to *Z* conformation change,[16] and the stability of drug-DNA complex.[17]

A qualitative weakness of MSPA that also arises in other simplified theoretical approaches[18] lies in the *a priori* nature of modes. Though effective elastic constants depend on temperature, normal modes indeed conserve a plane-wave structure.[12] As a consequence, dispersion relations for the normal modes are well defined as for phonons in crystals.[19] In other words, the coherence length is infinite and the momentum selection rule give rise to a discrete set of lines in the theoretical predictions for Raman spectra.[19] On the contrary, amorphous materials or more generally thermally disordered systems give rise to normal modes with short coherence lengths, whose power spectrum displays a finite width.[2,3,20] As a result, momentum selection rules break down and light-scattering processes may occur from essentially all normal modes.[21,22] Correspondingly, for a DNA molecule in solution, the Raman spectrum is continuous and does not depend on the wave length of the incident laser beam nor on the scattering angle.[7]

[a)]Electronic mail: cocco@lpt.ens.fr,
[b)]Electronic mail: monasson@lpt.ens.fr

Understanding the vibrations of a system in presence of thermal (or configurational) disorder is a difficult task.[23,24] Nonharmonicities in the interactions between constituents may modify deeply the usual phonon picture of wave propagation in solids, and generally forbid any rigorous analytical treatment of the dynamical equations. An interesting approach to circumvent this difficulty has been proposed in the context of liquid state dynamics.[25] The idea is to start from a randomly chosen configuration at thermodynamical equilibrium. Then, the equations of motion around this fixed initial configuration can be linearized, defining some instantaneous normal modes (INM) and their corresponding relaxation times, i.e., frequencies. All these quantities may then be averaged over the initial configuration chosen from the Gibbs ensemble at the desired temperature. This way, one obtains a precise description of the short-times dynamics based on the average spectrum of relaxation times and the statistical properties of the INM.[25] As a major advantage, the INM approach takes into account thermal disorder through the choice of the random initial configuration and gives rise to highly disordered normal modes with finite autocorrelation length as expected at finite temperature. Due to the linearization procedure, the information available through INM calculations is restricted to short-times dynamics. This limitation is however not serious in the range of frequencies mentioned above for DNA collective dynamics as we shall see later.

From a theoretical point of view, the calculation of the INM around a fixed initial configuration is a hard task that can be performed analytically for simple enough models only.[26–28] In this article we describe the hydrogen bond vibrations and the helicoidal (corresponding to twist angle as well as compression/stretching) fluctuations of a simple DNA model by normal modes that are not plane waves using the INM approach. We are able in particular to calculate the frequency dependent density of state at a given temperature, the coherence length of the normal modes, and some pseudo-dispersion relations at ambient temperature. The model that we consider has been introduced in a previous article to study the DNA denaturation driven by temperature or mechanically induced by a torque.[29] This study was motivated by the recent development of micromanipulation techniques[30,31] that have allowed the direct observation of DNA denaturation induced by an external torsional stress.[32,33] Our model describes the DNA molecule at the base pair level through three degrees of freedom: the base pair radius, its angle in the plane perpendicular to the molecular axis, and the height of the base pair along this axis. The potential energy is sufficiently simple to allow for sophisticated analytical calculations of normal collective modes. From a technical point of view, our calculation is inspired from a recent study of instantaneous modes in a one-dimensional disordered system[34] that mixes techniques used in localization theory (the resolvent calculation), disordered system (replica trick),[35] and a variational Gaussian wave function method. As we shall see, the interest of the calculation is two-fold. First, it gives theoretical predictions for the spectrum of modes, the effective dispersion relations, and damping width at ambient temperature that can be directly confronted with Raman spectroscopy and to neutron scattering data. Second, it is a way to check the validity of (and eventually improve) our model in very different experimental conditions from the ones it was originally designed for.

The article is organized as follows. In Sec. II, we define the DNA model and explain how to compute its statistical physics properties. The choice of the force constants and the main thermodynamical features are then exposed. Section III is devoted to dynamics and to the definition of the instantaneous modes. The relationship between the latter and Raman spectra is evoked. The analytical framework necessary to calculate the properties of INM is presented in Sec. IV. Results are given and compared to experiments in Sec. V. Finally, we present some conclusions and perspectives in Sec. VI.

II. PRESENTATION AND MAIN FEATURES OF THE DNA MODEL

In this section, we describe the DNA model under study and briefly recall how it can be studied using statistical mechanics techniques as well as its main thermodynamical features (see Ref. 29). We then analyze the dispersion relations and spectral density of the normal modes at zero temperature.

A. Definition of the model

Our model mainly aims at reproducing the double helical structure of DNA. There are different kinds of double helix geometries the most common of which are B-DNA, A-DNA, and Z-DNA; they depend greatly on environmental conditions e.g., degree of hydration, ionic concentration, etc. The B-DNA and A-DNA are both right-handed helices that correspond to different sugar puckering modes: $C_2'-endo$ for B family with a distance between adjacent phosphates along the molecular backbone of $L \simeq 7$ Å, $C_3'-endo$ for A-family with $L \simeq 5.9$ Å.[42] We focus on the Watson–Crick double helix structure (B-DNA) that a DNA molecule takes, e.g., in solution at ambient temperature and physiological conditions.

The model is schematized in Fig. 1, see also Ref. 36. Each base pair ($j=1,\ldots,N$) is described by its radius r_j, the angle φ_j in the plane perpendicular to the helical axis, and the height z_j along the latter. The sugar phosphate backbone is made of rigid rods, the distance between adjacent bases on the same strand being fixed to $L=7$ Å.[37] This backbone distance introduces a geometrical constraint between two successive base pairs, see Fig. 1,

$$\sqrt{(z_j-z_{j-1})^2+r_j^2+r_{j-1}^2-2r_jr_{j-1}\cos(\varphi_j-\varphi_{j-1})}=L, \quad (1)$$

that couples the degrees of freedom $r_j, r_{j-1}, \varphi_j, \varphi_{j-1}$, z_j, z_{j-1}. Identity (1) allows us to express $h_j=z_j-z_{j-1}$ as a function of r_j, r_{j-1} and of the twist angle $\theta_j=\varphi_j-\varphi_{j-1}$,

$$h_j(r_j,r_{j-1},\theta_j)=\sqrt{L^2-r_j^2-r_{j-1}^2+2r_jr_{j-1}\cos\theta_j}, \quad (2)$$

and to choose radii r_j and angles φ_j as independent degrees of freedom from which the heights z_j may be unambiguously

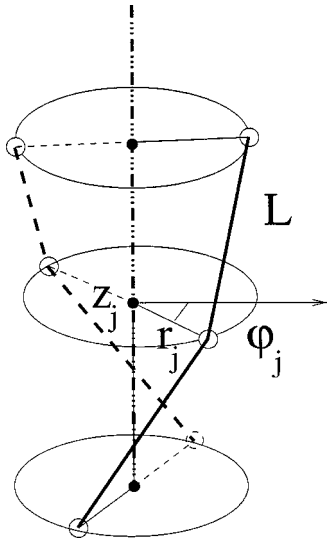

FIG. 1. The helicoidal DNA model: each base pair is modelized through its radius r_j, angle φ_j, and height z_j. The axial distance and twist angle between successive base pairs are, respectively, denoted by $h_j=z_j-z_{j-1}$ and $\theta_j=\varphi_j-\varphi_{j-1}$. The backbone length along the strands is fixed to L.

obtained. This choice is motivated by mathematical convenience only. We could have kept, e.g., r_j, z_j and eliminated φ_j as well.

The Hamiltonian V associated to a configuration of independent degrees of freedom $\{r_j,\varphi_j\}$ is the sum of three different contributions,

$$V[\{r_j,\varphi_j\}]=\sum_{j=1}^{N} V_m(r_j)+\sum_{j=2}^{N}\,(V_s(r_j,r_{j-1}) + V_b(r_j,r_{j-1},\varphi_j-\varphi_{j-1})), \tag{3}$$

that we now describe.

Hydrogen bonds inside a given pair n are taken into account through the short-range Morse potential[12,38]

$$V_m(r_j)=D\,(e^{-a(r_j-R)}-1)^2, \tag{4}$$

with $R=10$ Å. The width of the well amounts to $3a^{-1}\simeq 0.5$ Å,[39] in agreement with the order-of-magnitude of the relative motion of the hydrogen-bonded bases.[40] A base pair with diameter $r>r_d=R+6/a$ may be considered as open. The potential depth D, typically of the order of 0.1 eV (Ref. 12) depends on the base pair type [adenine–thymine (AT) or guanine–citosine (GC)] as well as on the ionic strength. Note that the Morse potential V_m increases exponentially with decreasing $r<R$ and may be considered as infinite for $r<r_{\min}=9.7$ Å.[41]

The vertical interaction between adjacent base pairs in the B-DNA conformation is accounted for by the stacking potential[42]

$$V_s(r_j,r_{j-1})=E\,e^{-b(r_j+r_{j-1}-2R)}(r_j-r_{j-1})^2. \tag{5}$$

Due to the decrease of molecular packing with base pair opening, the stiffness prefactor in Eq. (5) is exponentially attenuated and becomes negligible beyond a distance $\simeq 5b^{-1}=10$ Å, which coincides with the diameter of a base pair.[39]

An elastic energy depending on the axial distance h_j is introduced to describe the vibrations of the molecule in the B-phase,

$$V_b(r_j,r_{j-1},\theta_j)=K(h_j-H)^2. \tag{6}$$

The helicoidal structure arises from the choice of $H<L$: in the rest configuration $r_j=R$ at $T=0$ K, V_b is minimum and zero for the twist angle $\Theta>0$ with $\sin(\Theta/2)=\sqrt{L^2-H^2}/(2R)$. The above definition of V_b holds as long as the argument of the square root in Eq. (6) is positive, that is if r_j,r_{j-1},θ_j are compatible with rigid rods having length L. By imposing $V_b=\infty$ for negative arguments, unphysical values of r_j,r_{j-1},θ_j are excluded. As the behavior of a single strand ($r>r_d$) is uniquely governed by this rigid rod condition, the model does not only describe vibrations of helicoidal B-DNA but is also appropriate for the description of the denatured phase.[29]

B. Calculation of partition function

The configurational partition function at inverse temperature $\beta=1/(k_BT)$ reads

$$Z=\int_{r_{\min}}^{\infty} r_1\,dr_1\int_{-\infty}^{\infty}d\varphi_1\cdots\int_{r_{\min}}^{\infty} r_N\,dr_N\int_{-\infty}^{\infty}d\varphi_N \times\exp\{-\beta V[\{r_j,\varphi_j\}]\}\,\delta(\varphi_1)\prod_{j=2}^{N}\chi(\theta_j). \tag{7}$$

The angle of the first extremity of the molecule is set to $\varphi_1=0$ with no restriction due to the arbitrary choice of the angular reference axis, see Fig. 1, whereas the last one, φ_N, is not constrained. The χ factors entering Eq. (7) are defined by $\chi(\theta_j)=1$ if $0\leqslant\theta_j=\varphi_j-\varphi_{j-1}\leqslant\pi$, and 0 otherwise to prevent any clockwise twist of the chain to represent a right-handed helix. Partition function Z can be calculated using the transfer integral method,[43]

$$Z=\int_{r_{\min}}^{\infty} r_1\,dr_1\int_{r_{\min}}^{\infty} r_N\,dr_N\int_{-\infty}^{\infty}d\varphi_N\langle r_N,\varphi_N|T^N|r_1,0\rangle, \tag{8}$$

where the transfer operator entries read $\langle r,\varphi|T|r',\varphi'\rangle=T(r,r',\theta)$ with $\theta=\varphi-\varphi'$ and

$$T(r,r',\theta)=X(r,r')\,\exp\{-\beta V_b(r,r',\theta)\}\,\chi(\theta), \tag{9}$$

$$X(r,r')=\sqrt{rr'}\times\exp\left\{-\frac{\beta}{2}(V_m(r)+V_m(r'))-\beta V_s(r,r')\right\}. \tag{10}$$

At fixed r,r', the angular part of the transfer matrix T is translationally invariant in the angle variables φ, φ' and can be diagonalized through a Fourier transform. Thus, for each Fourier mode k we are left with an effective transfer matrix on the radius variables

$$T_k(r,r')=X(r,r')\,Y_k(r,r'), \tag{11}$$

with

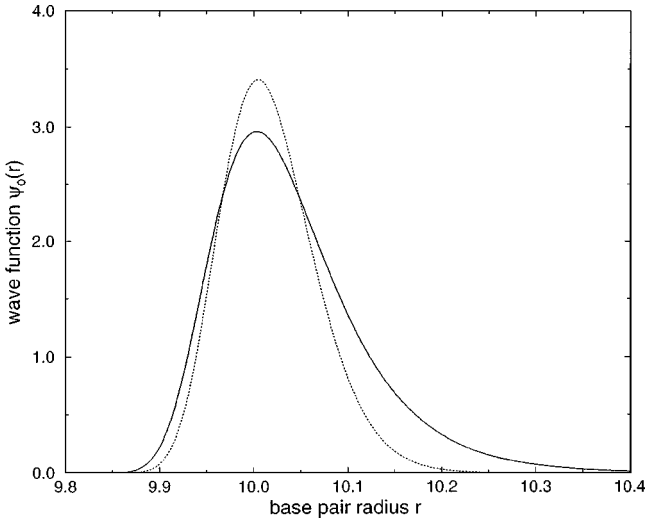

FIG. 2. Ground state wave functions $\psi_0(r)$ at $T=27\,^{\circ}\mathrm{C}$ for two choices of the energetic parameters: $D=0.15$ eV, $E=0.74$ eV/Å^2 (full curve) and $D=0.16$ eV, $E=4$ eV/Å^2 (dotted curve).

$$Y_k(r,r')=\int_0^{\pi} d\theta \exp\{-\beta V_b(r,r',\theta)-ik\theta\}. \tag{12}$$

The only mode contributing to Z is $k=0$ once φ_N has been integrated out in Eq. (7). In the $N\to\infty$ limit, the free-energy density f is simply given by $f=-k_BT\ln\lambda_0$, where λ_0 is the maximal eigenvalue of T_0 whose corresponding eigenvector will be denoted by $\psi_0(r)$.

C. Thermodynamical properties and parameters

The ground state wave function $\psi_0(r)$ is shown in Fig. 2 at ambient temperature $T=300$ K. It is entirely localized in the Morse potential well as expected for a DNA molecule in B-configuration. The first excited eigenstate of the transfer matrix has an excess free-energy ΔG with respect to ψ_0 and is delocalized: it extends over all values of $r>r_d$, vanishes for $r<r_d$, and thus represents a denatured molecule. At some higher temperature T_m, the bound wave function disappears and ψ_0 suddenly undergoes a delocalization transition. In other words, hydrogen bonds break up and T_m can be interpreted as the melting temperature.[29]

The values of the parameters entering the potential energy are discussed in Ref. 29 and are listed below:

inverse hydrogen bond length: $a=6.3$ Å^{-1}.
zero temperature interplane distance: $H=3$ Å.
Morse potential depth: $D=0.16$ eV.
attenuation coefficient for stacking interactions: $b=0.49$ Å^{-1}.
stacking stiffness: $E=4$ eV/Å^2.
axial elasticity constant: $K=0.014$ eV/Å^2.

The values of a and b have been borrowed from literature.[29] The choice of the other parameters D, E, K, H ensures that geometrical and thermodynamical properties as the average twist angle, the mean axial distance between successive bases in the B-conformation, the melting temperature $T_m=350$ K, and the denaturation free-energy ΔG are correctly predicted.[29]

TABLE I. Three choices of the depths of the Morse potential D and of the stacking stiffnesses E giving the desired melting temperature $T_m=350$ K. The corresponding denaturation free-energies ΔG are expressed in units of k_BT at $T=300$ K.

D (eV)	E (eV/Å^2)	ΔG (k_BT)
0.15	0.74	0.762
0.16	4	0.825
0.17	12	0.691

Notice that the main uncertainty in this tuning procedure arises with the choice of the stacking stiffness E. Three possible pairs of parameters (D,E) that correctly fit $T_m=350$ K are listed in Table I, as well as the corresponding denaturation free-energies ΔG at $T=300$ K. We have selected the pair giving the largest prediction for the denaturation free-energy that is in closest agreement with thermodynamical estimates of ΔG.[42] It can be easily seen from Table I that E varies much more than D and ΔG and is therefore less accurately predicted than the other parameters of the model.

III. DYNAMICS AND INSTANTANEOUS NORMAL MODES

Our aim is to perform an analytical calculation of the spectrum of molecular vibrations on characteristic time scale of the picoseconds and at ambient temperature. In this section, we first write the dynamical equations for the model. We then linearize these equations around a given (and randomly chosen) configuration of the thermally equilibrated system and define the instantaneous normal modes as the vibrations of the DNA molecule around this configuration. The density of instantaneous normal modes can be related to some extent to the Raman intensity. Finally, we consider the special case of zero temperature. The explicit calculation of the dispersion relations and the density of modes allows for a decoupling of the angular and radial motions in acoustic and optical modes, respectively. It also provides useful comparisons with the finite temperature results of Sec. V.

A. Dynamical equations for the DNA model

We denote the configuration of the molecule at time t by $\{r_j^t,\varphi_j^t\}$. The equations of motion read

$$\begin{aligned} m\ddot{r}_j^t &= mr_j^t(\dot{\varphi}_j^t)^2-\frac{1}{2}\frac{\partial V}{\partial r_j^t}, \\ m(r_j^t)^2\ddot{\varphi}_j^t &= -\frac{1}{2}\frac{\partial V}{\partial \varphi_j^t}, \end{aligned} \tag{13}$$

where the potential energy V has been defined in Eq. (3). The effective half-mass $m=300$ u.m.a. of a base pair takes into account the atomic constituents of the nucleotide and of the backbone as well as the primary hydration shell which is tightly bound to the base.[18,42,44] The size of the primary shell depends on the hydration degree and is of the order of 10-20 water molecules per nucleotide. The characteristic relaxation time of the primary shell is typically $\tau_1\simeq 10^{-10}$ s.[44] Therefore, for dynamical processes taking place on time scales

$\tau < \tau_1$, that is for frequencies $\nu > 0.3$ cm^{-1} primary shells may be considered as rigidly linked to the bases and simply taken into account through the effective mass m. Our choice for m is in close agreement with the mass considered by Volkov and Kosevich.[45] Taking into account the additional water shell mass and averaging over the possible bases A, T, G, and C, these authors have calculated some estimates of the masses of the nucleotide $m_n = 199$ u.m.a. and of the backbone elements $m_b = 109$ u.m.a. giving a total mass $m = m_n + m_b = 308$ u.m.a. per base.[45]

In addition to the primary shell, there exists a secondary hydration shell containing less rigidly bound water molecules. The characteristic time scale of relaxation of this secondary shell at ambient temperature is $\tau_2 \simeq 10^{-12}$ s,[44,46] that is of the same order-of-magnitude as in bulk water. Both water shells stabilize the DNA structure and their presence is taken into account in the force constants of the potential energy, Eq. (3). However, in the equations of motion, Eq. (13), the viscous damping of the molecule due to the solvent is not considered.

B. Linearization approximation and instantaneous modes

We linearize the equations of motions, Eq. (13) around a casual initial configuration $\mathcal{C} = \{r_j, \varphi_j\}$ of the system already in thermodynamical equilibrium, defining for each base pair j,

$$\begin{aligned} r_j^t &= r_j + y_j^t, \\ \varphi_j^t &= \varphi_j + \tilde{\phi}_j^t. \end{aligned} \tag{14}$$

Once linearized the dynamical Eqs. (13) are rewritten in terms of the displacement variables $y_j^t, \phi_j^t \equiv R.\tilde{\phi}_j^t$ and read

$$\begin{aligned} m\ddot{y}_j^t &= \sum_k (\mathcal{D}_r^{\mathcal{C}})_{j,k} y_k^t + \sum_k (\mathcal{D}_m^{\mathcal{C}})_{j,k} \phi_k^t, \\ m\ddot{\phi}_j^t &= \sum_k (\mathcal{D}_m^{\mathcal{C}})_{k,j} y_k^t + \sum_k (\mathcal{D}_\varphi^{\mathcal{C}})_{j,k} \phi_k^t, \end{aligned} \tag{15}$$

where

$$(\mathcal{D}_r^{\mathcal{C}})_{jk} = \frac{1}{2} \left. \frac{\partial^2 V}{\partial r_j \partial r_k} \right|_{\mathcal{C}},$$

$$(\mathcal{D}_m^{\mathcal{C}})_{jk} = \frac{1}{2R} \left. \frac{\partial^2 V}{\partial r_j \partial \varphi_k} \right|_{\mathcal{C}}, \quad \text{and} \quad (\mathcal{D}_\varphi^{\mathcal{C}})_{jk} = \frac{1}{2R^2} \left. \frac{\partial^2 V}{\partial \varphi_j \partial \varphi_k} \right|_{\mathcal{C}} \tag{16}$$

are the $N \times N$ matrices of second derivatives of the potential energy V around configuration $\mathcal{C}$. To solve the linear system, Eq. (15), one has to find the eigenvalues λ of the $2N \times 2N$ Hessian matrix

$$\mathcal{D}^{\mathcal{C}} = \begin{pmatrix} \mathcal{D}_r^{\mathcal{C}} & \mathcal{D}_m^{\mathcal{C}} \\ \mathcal{D}_m^{\mathcal{C}} & \mathcal{D}_\varphi^{\mathcal{C}} \end{pmatrix}. \tag{17}$$

It is important to notice that due to the dependence on the initial configuration $\mathcal{C}$ the elements of the matrix $\mathcal{D}^{\mathcal{C}}$ are not translationally invariant. Consequently, the eigenvectors of $\mathcal{D}^{\mathcal{C}}$, i.e., the instantaneous normal modes corresponding to the initial configuration $\mathcal{C}$ are not plane waves.

The eigenvalues histogram $\rho^{\mathcal{C}}(\lambda)$ give the density of the normal modes as a function of the initial configuration. The latter is distributed according to the Gibbs measure

$$\mathcal{P}(\mathcal{C} = \{r_j, \varphi_j\}) = \frac{1}{Z} \exp(-\beta V[\{r_j, \varphi_j\}]), \tag{18}$$

where V is the Hamiltonian defined in Eq. (3). Once averaged over distribution (18), the mean density of states $\rho(\lambda)$ is available and depends only on the temperature $T = 1/\beta$. The frequency spectrum $\rho_f(\nu)$ is straightforwardly obtained through the relationship, see Eq. (15),

$$\begin{aligned} \nu &= \frac{1}{2\pi} \sqrt{\frac{\lambda}{m}}, \\ \rho_f(\nu) &= 4\pi \sqrt{m\lambda}\ \rho(\lambda). \end{aligned} \tag{19}$$

To lighten notation, we shall drop the f subscript in Eq. (19) and use indifferently the same letter ρ to denote the density of states as a function of the eigenvalue λ or frequency ν.

The spectrum of the Hessian matrix, Eq. (17) is not necessarily positive. Some instantaneous modes may be unstable and grow with time within the linear approximation. Their corresponding eigenvalues λ are negative and the associated frequencies ν are purely imaginary. Following the conventions of Ref. 25, imaginary frequencies ν will be conveniently represented by minus their modulus $-|\nu|$, that is by points on the negative frequency semiaxis. We shall come back in Sec. V to these modes.

C. Relationship with Raman spectra

Raman scattering intensity is directly related to the density of normal modes. In disordered solids the coherence length of the normal modes is short compared to optical wavelengths, so the conservation of momentum is no longer a restrictive selection rule and does not give rise to a discrete set of lines for the spectrum. Light-scattering processes occur from essentially all the normal modes of the material and the spectra are continuous. As we will see later, the assumption of short coherence length is well verified in our model at finite temperature. The relationship between the Raman intensity $\mathcal{I}(\nu)$ and the density of normal modes $\rho(\nu)$ is generally expressed via the light-to-vibrations coupling coefficient $C(\nu)$,[21]

$$\mathcal{I}(\nu) = \rho(\nu) C(\nu) \left(\frac{n(\nu) + 1}{\nu} \right), \tag{20}$$

where

$$n(\nu) = \frac{1}{\exp\left(\dfrac{h\nu}{k_B T} \right) - 1} \tag{21}$$

is the average population of level ν. The spectral dependence of $C(\nu)$ is still an unsettled question. Early studies devoted to the relationship between Raman spectra and densities of modes assumed that the light-to-vibrations coupling was independent of frequency, i.e., $C(\nu) = 1$.[21] Later works conjec-

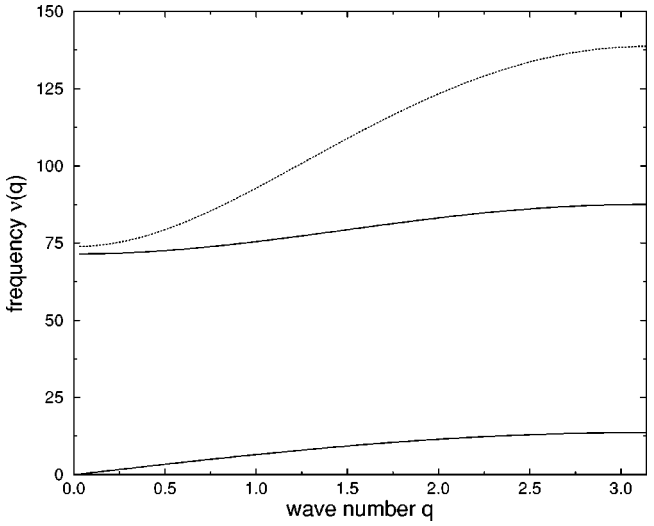

FIG. 3. Dispersion relations at zero temperature. From bottom to top: $\nu_\varphi(q)$ for acoustic modes, $\nu_r(q)$ for optical modes with two different choices of the parameters $D=0.15$ eV, $E=0.74$ eV/Å^2 (full curve) and $D=0.16$ eV, $E=4$ eV/Å^2 (dotted curve).

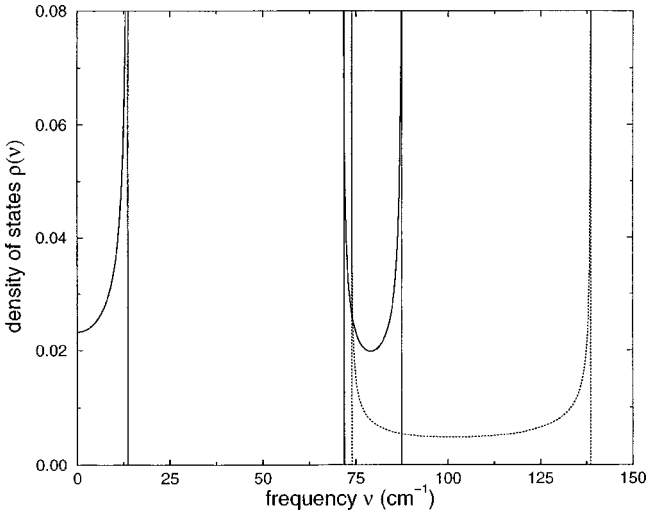

FIG. 4. Density of states at zero temperature. From left to right: acoustic modes spectrum $\rho_\varphi(\nu)$, optical modes spectra $\rho_r(\nu)$ for $D=0.15$ eV, $E=0.74$ eV/Å^2 (full curve), and $D=0.16$ eV, $E=4$ eV/Å^2 (dotted curve).

tured a quadratic behavior $C(\nu)\sim\nu^2$ at very low frequencies and a less steep increase for larger ν.[22] Recently, comparisons between neutron scattering experiments and calorimetric measures have given evidence for a linear dependence $C(\nu)\propto\nu$ for different glasses in the frequency range $8\ \mathrm{cm}^{-1}<\nu<100\ \mathrm{cm}^{-1}$,[47,48] the upper bound being related to the Debye frequencies of the corresponding crystals.

D. Normal modes at zero temperature

The linearized equations of motion at zero temperature are obtained performing an expansion of the potential energy V [Eq. (3)] up to the second order around the rest positions: $r_j^t=R+y_j^t$, $\varphi_j^t=j\Theta+\phi_j^t/R$:

$$\begin{aligned} m\,\ddot{y}_j^t &= -a^2 D y_j^t - K_{yy}(2y_j^t+y_{j+1}^t+y_{j-1}^t) \\ &\quad -E\,(2y_j^t-y_{j+1}^t-y_{j-1}^t)-K_{y\,\phi}(\phi_{j+1}^t-\phi_{j-1}^t), \\ m\,\ddot{\phi}_j^t &= -K_{\phi\phi}(2\phi_j^t-\phi_{j+1}^t-\phi_{j-1}^t)+K_{y\,\phi}(y_{j+1}^t-y_{j-1}^t), \end{aligned} \tag{22}$$

where

$$K_{yy}=(KR^2/H^2)(1-\cos\,\Theta)^2, \tag{23}$$

$$K_{\phi\phi}=(KR^2/H^2)(\sin^2\,\Theta), \tag{24}$$

$$K_{y\phi}=(KR^2/H^2)(\sin\Theta)(1-\cos\,\Theta). \tag{25}$$

The plane waves

$$\begin{pmatrix} y_j \\ \phi_j \end{pmatrix}=\begin{pmatrix} y_\pm(q) \\ \phi_\pm(q) \end{pmatrix}\exp\{i(qj-2\pi\nu_\pm(q)t)\} \tag{26}$$

are solutions of Eq. (22) with the relations of dispersion $\nu_\pm(q)$ shown in Fig. 3. Due to the difference of the order-of-magnitude between $a^2D=6.33$ eV Å^{-2}, $E=4$ eV Å^{-2} (or for the other choice of the parameters $a^2D=5.93$ eV Å^{-2}, $E=0.74$ eV Å^{-2}), and $K_{y\phi}=18\times10^{-3}$ eV Å^{-2}, $K_{yy}=6\times10^{-3}$ eV Å^{-2}, $K_{\phi\phi}=54\times10^{-3}$ eV Å^{-2}, it is clear that the angular and radial motions take place on two different time scales and become independent. The dispersion relations obtained when setting $K_{y\phi}=0$ and $K_{yy}=0$ are indistinguishable from the previous ones and read

$$\nu_r(q)\equiv\nu_+=\frac{1}{2\pi}\sqrt{\frac{a^2D}{m}+2\frac{E}{m}(1-\cos\,q)}, \tag{27}$$

$$\nu_\varphi(q)\equiv\nu_-=\frac{1}{2\pi}\sqrt{\frac{2K_{\phi\phi}}{m}(1-\cos\,q)}. \tag{28}$$

From the decoupling between angular and radial variables, Eqs. (27), (28) and Fig. 3, it appears that acoustic modes correspond to fluctuations of angular variables and optical modes correspond to fluctuations of radial variables. Note that transverse radial modes are of optical nature due the single site-dependent Morse potential representing hydrogen bonds. In our model, the degrees of freedom for the motions of the centers-of-mass of base pairs are not taken into account. Consequently no transverse acoustic modes are present.

The density of states $\rho(\nu)=1/(2\pi|\nu'(q)|)$ for each branch is given by

$$\rho_r(\nu)=\frac{4\pi\nu}{\sqrt{\left[(2\pi\nu)^2-\frac{a^2D}{m}\right]\left[\frac{a^2D+4E}{m}-(2\pi\nu)^2\right]}}, \tag{29}$$

$$\rho_\varphi(\nu)=\frac{1}{\sqrt{\frac{K_{\phi\phi}}{m}-(\pi\nu)^2}}\quad. \tag{30}$$

Note that the above densities are both normalized to 1/2 so that the total density of states $\rho_r(\nu)+\rho_\varphi(\nu)$ is properly normalized to unity. As shown in Fig. 4, Van Hove singularities are located at frequencies ν such that the denominators in Eq. (30) vanish, that is, stationary points of the dispersion relations (28).

E. Structure of the Hessian matrix

From the above considerations on the effective decoupling of radial and angular variables, $\mathcal{D}^{\mathcal{C}}_m$ will be set to zero hereafter. Therefore, the Hessian matrix, Eq. (17) is comprised of two $N\times N$ matrices, that is, the radial Hessian matrix $\mathcal{D}^{\mathcal{C}}_r$ and the angular Hessian matrix $\mathcal{D}^{\mathcal{C}}_\varphi$. In what follows, the notation $\mathcal{D}^{\mathcal{C}}$ will generically refer to either of these two matrices.

Because only nearest-neighbors along the molecule interact with each other, the Hessian matrix has a band diagonal structure,

$$(\mathcal{D}^{\mathcal{C}})_{kj}=\begin{cases} \frac{1}{2}d_0(r_j,r_{j-1},\theta_j)+\frac{1}{2}d_0(r_j,r_{j+1},-\theta_{j+1}) & \text{if} \quad k=j,\\ -\frac{1}{2}d_1(r_j,r_{j-1},\theta_j) & \text{if} \quad k=j-1,\\ -\frac{1}{2}d_1(r_{j+1},r_j,\theta_{j+1}) & \text{if} \quad k=j+1,\\ 0 & \text{if} \quad |k-j|\geqslant 2. \end{cases} \tag{31}$$

Explicit expressions of elements d_0 and d_1 are as follows:

For the radius Hessian matrix $\mathcal{D}^{\mathcal{C}}_r$, the elements

$$\begin{aligned} d_0(r,r')&=\frac{1}{2}\frac{d^2V_m}{dr^2}(r)+2E,\\ d_1(r,r')&=2E, \end{aligned} \tag{32}$$

do not depend on the twist θ. For simplicity, we have not considered the exponential attenuation term in V_s which is almost constant (and equal to unity) in the B-DNA phase. K_{yy} has been set to zero since it is three orders-of-magnitude smaller than other radial force constants.

For the angular Hessian matrix $\mathcal{D}^{\mathcal{C}}_\varphi$,

$$d_0(r,r',\theta)=d_1(r,r',\theta)=\frac{1}{R^2}\frac{d^2V_b}{d\theta^2}(r,r',\theta), \tag{33}$$

where the potential V_b has been defined in Eq. (6).

IV. ANALYTICAL FRAMEWORK

A. Definition of spectral quantities

We call $\lambda^{\mathcal{C}}_e$ (respectively, $w^{\mathcal{C}}_{a,e}$) the eigenvalues (respectively, the components of the associated eigenvectors normalized to unity) of $\mathcal{D}^{\mathcal{C}}$, with $e=1,\ldots,N$. Most spectral properties of $\mathcal{D}^{\mathcal{C}}$ can be obtained through the calculation of the resolvent[35]

$$G^{\mathcal{C}}_{ab}(\lambda+i\epsilon)=((\lambda+i\epsilon)\mathcal{I}-\mathcal{D}^{\mathcal{C}})^{-1}_{ab}=\sum_{e=1}^{N}\frac{w^{\mathcal{C}}_{a,e}w^{\mathcal{C}}_{b,e}}{\lambda-\lambda^{\mathcal{C}}_e+i\epsilon}, \tag{34}$$

where $\mathcal{I}$ denotes the identity operator.

Introducing the density of eigenvalues

$$\rho^{\mathcal{C}}(\lambda)=\frac{1}{N}\sum_{e=1}^{N}\delta(\lambda-\lambda^{\mathcal{C}}_e), \tag{35}$$

we may rewrite the discrete sum over eigenstates e in Eq. (34) as an integral over eigenvalues with measure $\rho^{\mathcal{C}}$. The knowledge of the trace of the resolvent,

$$\begin{aligned} \frac{1}{N}\sum_{a=1}^{N}G^{\mathcal{C}}_{aa}(\lambda+i\epsilon)&=\frac{1}{N}\sum_{e=1}^{N}\frac{1}{\lambda-\lambda^{\mathcal{C}}_e+i\epsilon}\\ &=\int_{-\infty}^{\infty}d\mu\ \frac{\rho^{\mathcal{C}}(\mu)}{\lambda-\mu+i\epsilon}, \end{aligned} \tag{36}$$

gives then access to the density of states through identity

$$\rho^{\mathcal{C}}(\lambda)=-\frac{1}{\pi}\lim_{\epsilon\to 0^+}\mathrm{Im}\left[\frac{1}{N}\sum_{a=1}^{N}G^{\mathcal{C}}_{aa}(\lambda+i\epsilon)\right]. \tag{37}$$

Another quantity of interest is the autocorrelation function of eigenvectors at distance d,

$$A^{\mathcal{C}}_e(d)=\sum_{a=1}^{N-d}w^{\mathcal{C}}_{a,e}w^{\mathcal{C}}_{a+d,e}. \tag{38}$$

We then define $A^{\mathcal{C}}(\lambda,d)$ as the average value of $A^{\mathcal{C}}_e(d)$ over all eigenvectors e lying in the range $\lambda\leqslant\lambda^{\mathcal{C}}_e\leqslant\lambda+d\lambda$. This autocorrelation function is simply related to the off-diagonal resolvent, Eq. (34), through

$$\frac{1}{N}\sum_{a=1}^{N-d} G^{\mathcal{C}}_{a,a+d}(\lambda+i\epsilon)=\int_{-\infty}^{\infty} d\mu \ \frac{\rho^{\mathcal{C}}(\mu)}{\lambda-\mu+i\epsilon} \ A^{\mathcal{C}}(\mu,d), \tag{39}$$

that generalizes Eq. (36) to nonzero values of d. Taking the imaginary part of Eq. (39), we obtain

$$\rho^{\mathcal{C}}(\lambda) \ A^{\mathcal{C}}(\lambda,d)=-\frac{1}{\pi}\lim_{\epsilon\to 0^+}\mathrm{Im}\left[\frac{1}{N}\sum_{a=1}^{N-d} G^{\mathcal{C}}_{a,a+d}(\lambda+i\epsilon)\right]. \tag{40}$$

Therefore, the calculation of the large distance d behavior of $G^{\mathcal{C}}_{a,a+d}(\lambda+i\epsilon)$ will give access to the asymptotic scaling of the autocorrelation function

$$A^{\mathcal{C}}(\lambda,d)\propto(e^{-\sigma^{\mathcal{C}}(\lambda)+i \ q^{\mathcal{C}}(\lambda)})^d, \tag{41}$$

and thus to some effective relation of dispersion $\lambda^{\mathcal{C}}(q)$ and to the coherence length $1/\sigma^{\mathcal{C}}(\lambda)$ of the instantaneous modes at finite temperature.

B. Average over the instantaneous molecular configuration

To perform the average over the molecule configurations $\mathcal{C}$, we first rewrite the resolvent, Eq. (34) as the propagator of a replicated Gaussian field theory,[35]

$$\begin{aligned} G^{\mathcal{C}}_{ab}(\lambda+i\epsilon)&=\frac{-i\int\prod_{j=1}^{N} dx_j (x_a x_b)\exp\left(\frac{i}{2}(\lambda+i\epsilon)\sum_{j=1}^{N} x_j^2-\frac{i}{2}\sum_{j,k=1}^{N}\mathcal{D}^{\mathcal{C}}_{j,k} \ x_j x_k\right)}{\int\prod_{j=1}^{N} dx_j \exp\left(\frac{i}{2}(\lambda+i\epsilon)\sum_{j=1}^{N} x_j^2-\frac{i}{2}\sum_{j,k=1}^{N}\mathcal{D}^{\mathcal{C}}_{jk} \ x_j x_k\right)} \\ &=\lim_{n\to 0}-\frac{i}{n}\int\prod_{j=1}^{N} d\vec{x}_j(\vec{x}_a\cdot\vec{x}_b) \ \exp\left(\frac{i}{2}(\lambda+i\epsilon)\sum_{j=1}^{N}\vec{x}_j^2-\frac{i}{2}\sum_{j,k=1}^{N}\mathcal{D}^{\mathcal{C}}_{jk} \ \vec{x}_j\cdot\vec{x}_k\right). \end{aligned} \tag{42}$$

Replicated fields $\vec{x}_j=(x_j^1,\ldots,x_j^n)$ are n-dimensional vector fields attached to each site j. The positivity of ϵ ensures that the Gaussian integrals in Eq. (42) are well-defined.

At equilibrium, the molecular configuration $\mathcal{C}$ is drawn according to the Gibbs measure, Eq. (18). We shall denote the average of any quantity over distribution (18) in the same way as its configuration dependent counterpart but without $\mathcal{C}$ subscript. For instance, the average resolvent reads:

$$\begin{aligned} G_{ab}(\lambda+i\epsilon)=&\int_{r_{\min}}^{\infty} r_1 \ dr_1\int_{-\infty}^{\infty} d\varphi_1\cdots\int_{r_{\min}}^{\infty} r_N \ dr_N \\ &\times\int_{-\infty}^{\infty} d\varphi_N \mathcal{P}(\{r_j,\varphi_j\})G_{ab}^{\{r_j,\varphi_j\}}(\lambda+i\epsilon), \end{aligned} \tag{43}$$

where $\mathcal{P}$ is the Gibbs measure, Eq. (18). It is important to keep in mind that $\mathcal{D}^{\mathcal{C}}_{jk}$ vanishes for $|j-k|\geq 2$, see Sec. III B. Therefore, only replicated variables $\vec{x}_j,\vec{x}_k$ corresponding to adjacent base pairs along the molecule $(j=k\pm 1)$ interact together in the expression (42) of the resolvent.

C. Transfer matrix formalism

The one-dimensional structure of the interactions in Eq. (43) can be exploited through the introduction of a transfer matrix $\mathcal{T}$ relating the molecular variables r_j,φ_j as well as the replicated variables $\vec{x}_j$ to their counterparts at site $j-1$. The entries of this matrix can be read from Eqs. (3), (42), (43),

$$\begin{aligned} \langle r,\varphi,\vec{x}|\mathcal{T}\,|r',\varphi',\vec{x}'\rangle=T(r,r',\theta)\exp\Bigg(&\frac{i}{4}(\lambda+i\epsilon) \\ &\times(\vec{x}^2+\vec{x}'^2)-\frac{i}{4}d_0(r,r',\theta)\vec{x}^2 \\ &-\frac{i}{4}d_0(r',r,-\theta)\vec{x}'^2 \\ &+\frac{i}{2} \ d_1(r,r',\theta)\vec{x}\cdot\vec{x}'\Bigg). \end{aligned} \tag{44}$$

In the above expression, d_0 and d_1 are, respectively, the diagonal and off-diagonal elements of $\mathcal{D}^{\mathcal{C}}$, see Eq. (31), while T has been defined in Eq. (10). Notice that $\mathcal{T}$ is a symmetric (but not Hermitian) matrix.

By definition, the average resolvent G_{ab} is the correlation function of replicated variables $\vec{x}_a$ and $\vec{x}_b$, Eq. (42). Within the transfer matrix formalism, this mean-dot product can be computed from the knowledge of eigenvalues Λ_l and all (normalized) eigenvectors $\Psi_l(r,\varphi,\vec{x})$ of $\mathcal{T}$. Calling d the axial distance $|a-b|$ between sites a and b along the molecule, the average resolvent reads in the thermodynamical limit

$$G_{ab}(\lambda+i\epsilon)$$
$$=\lim_{n\to 0}-i\sum_{l=0}^{\infty}\left(\frac{\Lambda_l}{\Lambda_0}\right)^d$$
$$\times\left[\int d\vec{x}\ dr\ d\varphi\ x^1\ \Psi_0(r,\varphi,\vec{x})\ \Psi_l(r,\varphi,\vec{x})\right]^2. \quad (45)$$

The maximal eigenvalue (in modulus) of $\mathcal{T}$ coincides with $l=0$ and increasingly excited states correspond to $l\geqslant 1$.

The average diagonal resolvent G_{aa} and thereby the mean density of states may be obtained from Eq. (45) when $d=0$,

$$\rho(\lambda)=\frac{1}{\pi}\lim_{\epsilon\to 0^+,n\to 0}\mathrm{Re}\left[\int d\vec{x}\ dr\ d\varphi\ \Psi_0(r,\varphi,\vec{x})^2\ (x^1)^2\right]. \quad (46)$$

Expression (45) may also be used to compute the autocorrelation function of eigenvectors at large distances d, for which the resolvent Eq. (43) scale asymptotically as [see Eq. (41)],

$$G_{a,a+d}(\lambda+i\epsilon)\propto\exp(-\sigma(\lambda)\ d+i\ q(\lambda)\ d), \quad (47)$$

where both $\sigma(\geqslant 0)$ and q depend on the energy level λ. When d is large, the sum in Eq. (45) is dominated by the $l=1$ contribution and Eq. (47) may be reformulated as

$$\lim_{d\to\infty}\frac{1}{d}\ \ln G_{a,a+d}(\lambda+i\epsilon)=-\sigma(\lambda)+i\ q(\lambda), \quad (48a)$$
$$=\lim_{n\to 0}\ln\left(\frac{\Lambda_1}{\Lambda_0}\right), \quad (48b)$$

which allows to derive σ and q from the knowledge of Λ_0 and Λ_1. We shall explicitly compute the inverse length σ and wave number q in Sec. V and compare them to the zero temperature results of Sec. II D.

Notice that σ and q defined in Eq. (47) do not exactly coincide with the values of $\sigma^{\mathcal{C}}$ and $q^{\mathcal{C}}$ appearing in Eq. (41) averaged over $\mathcal{C}$ with distribution (18). To obtain the latter, one should average the logarithm of the resolvent $G^{\mathcal{C}}$ (quenched average) and not simply compute the logarithm of the mean resolvent as in Eq. (48a) (annealed average).[49] Due to concavity of the logarithm function, σ defined in Eq. (48a) is not only an approximation but also a lower bound to the average value of $\sigma^{\mathcal{C}}$. Comparison with numerical simulations made for the so-called ''smallworld'' lattice have shown that σ provides a very good estimate of the mean $\sigma^{\mathcal{C}}$.[34] To sum up, we can compute from the average resolvent G an upper bound $1/\sigma$ to the coherence length of the eigenvectors at level λ as well as an estimate q of their typical wave number.

D. Rayleigh–Ritz formula and variational approach

The diagonalization of the transfer matrix and the analytical continuation in $n\to 0$ could in principle be performed exactly due to the rotational invariance of $\mathcal{T}$ in the n-dimensional space of replicated variables. To avoid this tedious calculation, we resort to a Gaussian variational approach whose accuracy and reliability has been recently validated in the case of diffusion on random lattices.[27,34]

We start from the Rayleigh–Ritz formula for the largest eigenvalue Λ_0 of a (real-valued) matrix $\mathcal{T}$,

$$\Lambda_0=\max_{\Psi\neq 0}\mathcal{R}(\Psi), \quad (49)$$

where

$$\mathcal{R}(\Psi)=\frac{\langle\Psi|\mathcal{T}|\Psi\rangle}{\langle\Psi|\Psi\rangle}. \quad (50)$$

A lower bound Λ_0^g to Λ_0 can be obtained through maximization of the r.h.s. of Eq. (50) within a suitable trial family of wave functions $\Psi_0^g(Q)$ parametrized by some tunable variables Q. According to Eqs. (49), (50), we obtain

$$\Lambda_0^g=\mathcal{R}(\Psi_0^g(Q_{\mathrm{opt}})), \quad (51)$$

where the optimal parameter Q_{opt} is the solution of

$$\frac{d\mathcal{R}(\Psi_0^g(Q))}{dQ}\Big|_{Q=Q_{\mathrm{opt}}}=0. \quad (52)$$

Notice that within formulations (51), (52), $\mathcal{T}$ needs no longer to be real-valued and can assume complex values.

Hereafter, we apply this procedure to the transfer matrix (44) and resort to the following ansatz (prior to normalization),

$$\Psi_0^g(r,\varphi,\vec{x})=\psi_0(r)\exp\left(\frac{i}{4}\ Q(r)\vec{x}^2\right), \quad (53)$$

where $\psi_0(r)$ is the maximal wave function of the T_0 transfer matrix (11) of Sec. II B. This choice ensures that the correct eigenvalue λ_0 is recovered when the number of replicas n strictly equals zero: $\Lambda_0(n)=\lambda_0+O(n)$. The $\vec{x}$ dependence of the trial wave function, Eq. (53) results from the similarity of the operator $\mathcal{T}$ [Eq. (44)] with the transfer matrix of a 1D chain of interacting spherical spins, for which the ground state wave function is Gaussian.[43] Furthermore, this ansatz allows for an exact calculation of the n-dimensional integral over $\vec{x}$ and an easy continuation of the result to real values of n. Note here that the wave function Eq. (53) does not depend on φ. This is no assumption for $n=0$, see Sec. II B, and is supposed to give quantitatively good results for $n>0$.

The calculation of the Rayleigh–Ritz functional $\mathcal{R}$, Eq. (50) with the Gaussian ansatz, Eq. (53) is exposed in the Appendix. The resulting functional optimization equation over Q reads

$$\frac{\lambda_0\psi_0(r)}{2Q(r)}=\int_{r_{\min}}^{\infty}dr'\int_0^{\pi}d\theta T(r,r',\theta)\psi_0(r')$$
$$\times\frac{Q(r')+\lambda+i\epsilon-d_0(r',r,-\theta)}{\mathcal{W}(r,r',\theta)}, \quad (54)$$

where

$$\mathcal{W}(r,r',\theta)=(Q(r)+\lambda+i\epsilon-d_0(r,r',\theta))(Q(r')+\lambda$$
$$+i\epsilon-d_0(r',r,-\theta))-d_1(r,r',\theta)^2. \quad (55)$$

The solution of the above equation gives access to the variational estimate of the density of modes from Eq. (46),

$$\rho^g(\lambda) = -\frac{1}{\pi}\int_{r_{\min}}^{\infty} dr\, \psi_0(r)^2 \mathrm{Im}\left(\frac{1}{Q(r)}\right). \tag{56}$$

We can pursue the procedure to compute the excited eigenvalues Λ_l of $\mathcal{T}$. Drawing our inspiration from the 1D spherical spins chain transfer matrix,[43] we look for a variational wave function of the type

$$\Psi_l^g(r,\varphi,\vec{x}) = \Psi_0^g(r,\varphi,\vec{x}) P_l^g(x^1, x^2, \ldots, x^n), \tag{57}$$

where P_l^g is a polynomial of n variables of total degree l. To obtain the asymptotic behavior of the resolvent, Eq. (47), we only need the first excited state $l=1$, whose corresponding variational polynomial is clearly $P_1^g(\vec{x}) = x^1$, giving thereby from Eq. (50),

$$\tau^g = \frac{\Lambda_1^g}{\Lambda_0^g} = -2\left\{ \int_{r_{\min}}^{\infty} dr\, dr' \int_0^{\pi} d\theta T(r,r',\theta) \times \psi_0(r)\psi_0(r')\frac{d_1(r,r',\theta)}{\mathcal{W}(r,r',\theta)}\right\} \times \left\{ \lambda_0 \int_{r_{\min}}^{\infty} dr\, \psi_0(r)^2 Q(r)^{-1}\right\}^{-1}, \tag{58}$$

in the $n\to 0$ limit as shown in the Appendix.

V. RESULTS AND COMPARISON WITH EXPERIMENTS

A. Numerical resolution of the self-consistent equations

We first compute the ground state wave function $\psi_0(r)$ and the corresponding eigenvalue λ_0, see Sec. II B, by means of Kellog's method.[29] The integration range $[r_{\min}; r_{\max}]$ over r is discretized into a set of n_r points r_α, $\alpha = 1, \ldots, n_r$ with $r_1 = r_{\min} = 9.8$ Å and $r_{n_r} = r_{\max} = 10.7$ Å.

Self-consistent Eq. (54) for $Q(r)$ can then be solved iteratively. As can be checked at zero temperature, convergence is improved by iterating the equation for $1/Q(r)$ rather than for $Q(r)$ itself. We stop the iteration process as soon as the differences between the $1/Q(r_\alpha)$'s and their images through the iteration become smaller than 10^{-7} for all $1 \leqslant \alpha \leqslant n_r$.

Numerical difficulties come from the limits $\epsilon \to 0$ and $n_r \to \infty$. This can be best seen for base pairs vibrations in the simplest case $E=0$. The exact solution to Eq. (54) is $Q(r) = \lambda + i\epsilon - \frac{1}{2}V_m''(r)$. In other words, eigenvalues λ and radii r are in simple correspondence: to any permitted eigenvalue λ is associated one (or a few) radius $r(\lambda)$ such that $\lambda = \frac{1}{2}V_m''(r(\lambda))$ and the density of states reads

$$\rho(\lambda) = \lim_{\epsilon\to 0}\frac{1}{\pi}\int_{r_{\min}}^{r_{\max}} dr \frac{\psi_0(r)^2\epsilon}{\left(\lambda - \frac{1}{2}V_m''(r)\right)^2 + \epsilon^2} = \frac{2}{|V'''(r(\lambda))|}\,\psi_0(r(\lambda))^2. \tag{59}$$

In practice however, the integral in (59) is discretized as follows:

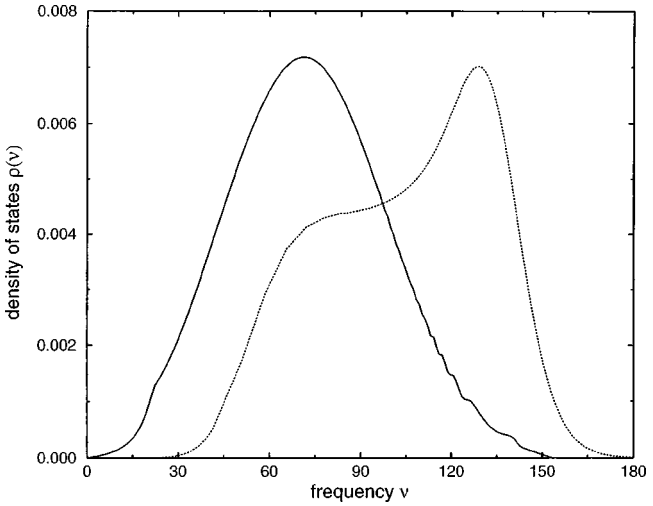

FIG. 5. Spectra $\rho_r(\nu)$ for optical modes at temperature $T = 27\,^\circ$C. Parameters are: $D = 0.15$ eV, $E = 0.74$ eV/Å^2 (full curve) and $D = 0.16$ eV, $E = 4$ eV/Å^2 (dotted curve). Each spectrum is normalized to one-half. Note the small oscillations on the tails of the curves due to numerical artifacts, see Sec. V A.

$$\rho(\lambda) = \lim_{\epsilon\to 0}\frac{1}{\pi}\sum_{\alpha=1}^{n_r} \frac{\psi_0(r_\alpha)^2\epsilon}{\left(\lambda - \frac{1}{2}V_m''(r_\alpha)\right)^2 + \epsilon^2}. \tag{60}$$

Consider the eigenvalue λ_γ corresponding to radius r_γ for some arbitrary integer γ. Dominant $O(1/\epsilon)$ contributions to the density $\rho(\lambda_\gamma)$ in Eq. (60) come from α in the range $\gamma - \Delta \leqslant \alpha \leqslant \gamma + \Delta$ with $\Delta \simeq 2n_r\epsilon/V'''(r_\gamma)$. Problems arise when Δ is close to unity. When λ scans the interval $[\lambda_\gamma; \lambda_{\gamma+1}]$, the index of the only (for $\Delta = 1$) contributing term to $\rho(\lambda)$ jumps from $\alpha = \gamma$ to $\alpha = \gamma + 1$ at some intermediate λ which will be a local minimum of the density ρ. Such local fluctuations are pure artifacts of the discretization procedure and must be removed by keeping $\Delta \gg 1$, that is $1/n_r \ll \epsilon \ll 1$. Typical suitable values of the parameters are $\epsilon = 2\times 10^{-2}$, $n_r = 4\times 10^3$, giving a spectrum $\rho(\lambda)$ almost normalized to unity (with a small error $\simeq \epsilon$).

Note that the same reasoning holds for the numerical calculation of the spectrum related to the angular Hessian matrix. The discretization of the integral over $0 < \theta < \pi$ must be replaced by a sum involving a large number $n_\theta = 900$ of terms to reach a good accuracy of the results.

B. Optical modes

Optical mode spectra (analytically obtained from the radius Hessian matrix) are displayed in Fig. 5 for different choices of D and E. They exhibit smooth shapes and Van Hove divergences have been smeared out by thermal disorder, compare to Fig. 4. As at zero temperature, the overall width of the spectrum is an increasing function of E.

For $E = 4$ eV/Å^2, the general form of $\rho(\nu)$ is reminiscent of the density of states at zero temperature, with a shoulder in $\nu_- \simeq 75$ cm^{-1} and a maximum in $\nu_+ \simeq 135$ cm^{-1}, in correspondence with the edges of the zero temperature spectrum, $\nu_-^0 = 73.8$ cm^{-1} and $\nu_+^0 = 138.7$ cm^{-1}. A careful analysis even shows a quantitative agreement between the

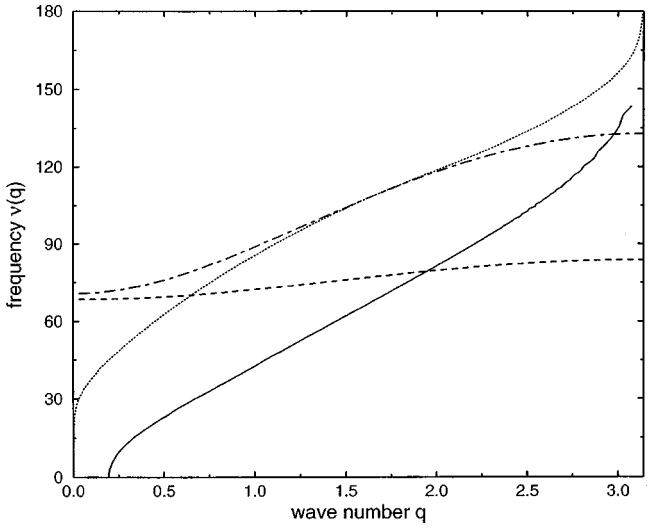

FIG. 6. Dispersion relations $\nu_r(q)$ for optical modes at temperature $T=27\,^{\circ}\mathrm{C}$. Parameters are: $D=0.15$ eV, $E=0.74$ eV/Å^2 (full curve) and $D=0.16$ eV, $E=4$ eV/Å^2 (dotted curve). For comparison, dispersion relations at zero temperature are recalled ($E=0.74$ eV/Å^2: dashed curve, $E=4$ eV/Å^2: dash-dotted curve).

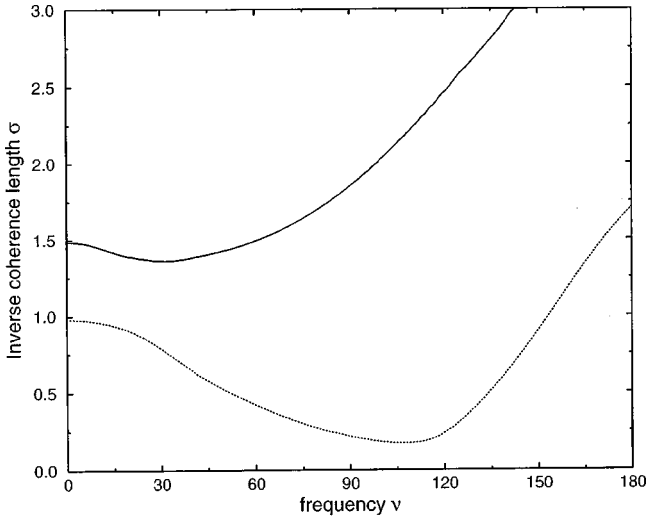

FIG. 7. Inverse coherence length $\sigma_r(\nu)$ for optical modes at temperature $T=27\,^{\circ}\mathrm{C}$. Parameters are: $D=0.15$ eV, $E=0.74$ eV/Å^2 (full curve) and $D=0.16$ eV, $E=4$ eV/Å^2 (dotted curve).

density of states at $T=300$ K and $T=0$ K for frequencies lying in the range $110\ \mathrm{cm}^{-1}<\nu<130\ \mathrm{cm}^{-1}$. A similar behavior, that is the robustness of the central part of the spectrum to (weak) disorder was also observed in Ref. 34.

At a weaker stiffness $E=0.74$ eV/Å^2, a single bump is observed. The range of allowed frequencies at zero temperatures $\nu_-^0=71.5\ \mathrm{cm}^{-1}<\nu<87.5\ \mathrm{cm}^{-1}$ is indeed too narrow and both peaks merge under the action of thermal disorder. Note that a very small fraction of modes seem to be unstable and give rise to imaginary frequencies, see Sec. III B. We however discard them since their integrated sum is smaller than the accuracy ϵ of the calculation.

Figure 6 shows the dispersion relations at ambient temperature for optical modes. The frequency $\nu_r(q)$ is an increasing function of the wave number over the interval $0\leqslant q\leqslant\pi$. Since the range of allowed frequencies is much larger at $T=300$ K than at $T=0$ K, there is no general coincidence with the zero temperature dispersion relations as can be seen for $E=0.74$ eV/Å^2. For larger stiffness constants, the dispersion relations for both temperatures however coincide for medium wave numbers, i.e., when $1\leqslant q\leqslant 2$ roughly. In agreement with the above analysis of the density of states, the effective thermal disorder gets weaker and weaker as the stiffness constant E grows.

When E increases, the molecule becomes more and more rigid since radii r_j less and less fluctuate from base pair to base pair. The wave function $\psi_0(r)$ gets more and more concentrated around the minimum of the Morse potential $r=R$, see Fig. 2 and the region of integration over r that mostly contributes to the density of states in Eq. (56) becomes narrower and narrower. On the opposite, for small E, $\psi_0(r)$ mainly reflects the structure of the Morse well whose flanks are not accessible at zero temperature. The tails of ψ_0 are large and give rise to some tails for the density of states. The cross-over between both regimes takes place at $E\sim D\ \ a^2$, that is of the order of a few eV/Å^2.

The inverse coherence length σ_r is plotted in Fig. 7 as a function of frequency. In the central region of the spectra, the corresponding autocorrelation lengths are $\xi\simeq 0.7$ for $E=0.74$ and $\xi\simeq 4$ for $E=4$ with a more sensitive dependence on ν in the latter case. As expected from the above discussion, ξ increases with E. The values of the coherence length ξ are in good agreement with the equilibrium correlation distance ζ defined through

$$\langle (r_j-\langle r\rangle)(r_{j+d}-\langle r\rangle)\rangle\propto e^{-d/\zeta},\quad (d\to\infty). \tag{61}$$

A thermodynamical calculation of ζ can be carried out from the knowledge of the excited states of the transfer matrix T_0 confined to the Morse potential.[50] Results are $\zeta\simeq 0.51$ for $E=0.74$ and $\zeta\simeq 0.93$ for $E=4$.[50] Note that ζ is the inverse damping width of the static structure factor whereas $\xi(\nu)$ is an energy (frequency) dependent coherence length.

C. Acoustic modes

We now turn to the acoustic spectrum (which is mathematically obtained from the angular Hessian matrix). The density of modes is shown on Fig. 8. We first concentrate on positive, that is real frequencies. The band edge $\nu_+^0=13.6\ \mathrm{cm}^{-1}$ of the zero temperature spectrum visible on Fig. 4 disappears at finite temperature. A sharp maximum now takes place at $\nu_M\simeq 7\ \mathrm{cm}^{-1}$. The width of the peak is smaller than for optical modes and can be estimated to $\Delta\nu\simeq 15\ \mathrm{cm}^{-1}$.

The densities of states at $E=0.74$ and $E=4$ coincide within 0.1%. We have numerically checked that the acoustic mode spectrum depends extremely weakly on the stiffness constant E over the whole range $0\leqslant E\leqslant\infty$. In other words, unlike optical modes, acoustic modes are not sensitive to the width of the ground state wave function ψ_0, i.e., to fluctuations of the base pair radius r, see Fig. 2. This observation is supported by inspection of the variational parameter $Q(r)$

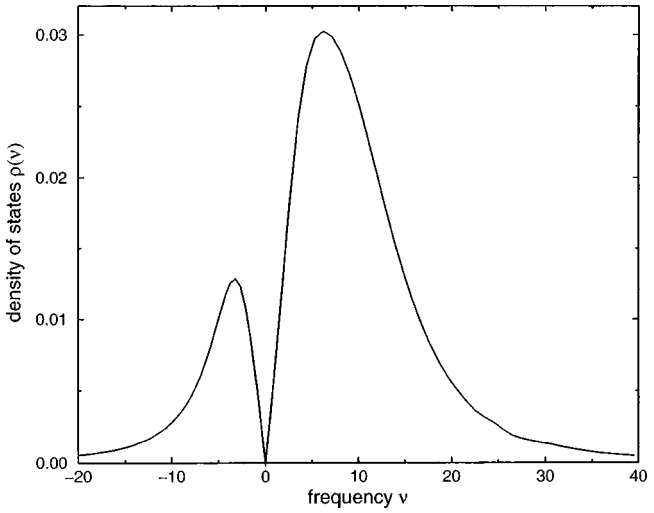

FIG. 8. Spectra $\rho_\varphi(\nu)$ for acoustic modes for $D=0.16$ eV, $E=4$ eV/Å^2. The curve for $D=0.15$ eV, $E=0.74$ eV/Å^2 is indistinguishable from the latter and from the approximation, Eqs. (63), (64), (65). The spectrum is normalized to one-half. Negative frequencies represent unstable modes according to the convention exposed in Sec. III B.

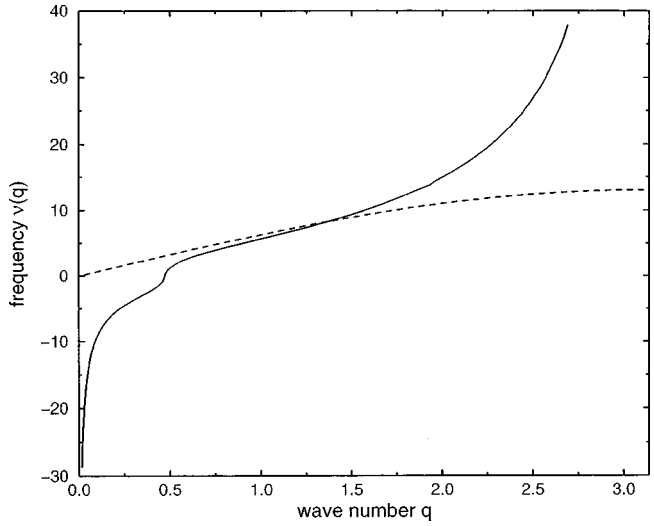

FIG. 9. Dispersion relation $\nu_\varphi(q)$ for acoustic modes (full curve). For comparison, the dispersion relation at zero temperature is recalled (dashed curve). Negative frequencies represent unstable modes according to the convention exposed in Sec. III B. Note the inflection point at $\nu=0$ due to this representation, see Sec. V C.

entering wave function (53). At fixed frequency, both imaginary and real parts of $Q(r)$ are indeed almost constant on the whole range of radius 9.8 Å$<r<$10.7 Å.

The robustness of the spectrum displayed in Fig. 8 can be understood by looking at the variations of $d_0(r,r',\theta)$ around the thermal average positions $r=r'=\langle r_n\rangle$ and $\theta=\langle\theta_n\rangle$. The second derivative of d_0 with respect to r at fixed twist angle equals $\partial_r^2 d_0 \simeq 0.045$ eV/Å^4 while the range of fluctuations of r is given by the largest squared width of ψ_0 (corresponding to $E=0$) and reads $\Delta\langle r_n^2\rangle \simeq 0.04$ Å^2. Therefore the fluctuations of the radius r modifies d_0 by $\frac{1}{2}\partial_r^2 d_0 \cdot \Delta\langle r_n^2\rangle \simeq 0.001$ eV/Å^2, that is by less than 2% of d_0 typically. Repeating the same calculation for twist-induced fluctuations, we obtain $\partial_\theta^2 d_0 \simeq 20$ eV/Å^2 and $\Delta\langle\theta_n^2\rangle \simeq k_B T/(d_0 R^2) \simeq 0.005$ rad^2. The resulting variations of d_0 due to changes of twist are of the order of $\frac{1}{2}\partial_\theta^2 d_0 \cdot \Delta\langle\theta_n^2\rangle \simeq 0.05$ eV/Å^2 that is comparable to d_0.

Consequently, an excellent approximation of the acoustic spectrum may be obtained by the following simple argument. Let us call

$$d_0(\theta) = \frac{1}{R^2}\,\frac{d^2 V_b}{d\theta^2}(R,R,\theta) \tag{62}$$

the diagonal element of $\mathcal{D}^{\mathcal{C}}$, Eq. (31), where we have for simplicity identified $\langle r_n\rangle$ with R since $\langle r_n\rangle - R \simeq 0.01$ Å$\ll R$ at $T=300$ K. The twist angle θ is approximately distributed with the Gibbs measure, see Eq. (12),

$$p(\theta) = \frac{1}{Y_0(R,R)}\exp\{-\beta V_b(R,R,\theta)\}. \tag{63}$$

Then we may substitute the variational Eq. (54) on $Q(r)$ with

$$\frac{1}{2\,Q} = \int_0^\pi d\theta\, p(\theta)\,\frac{Q+\lambda+i\epsilon-d_0(\theta)}{(Q+\lambda+i\epsilon-d_0(\theta))^2-d_0(\theta)^2}, \tag{64}$$

which involves a single parameter Q. Solving Eq. (64), the density of acoustic modes equals $-\mathrm{Im}(1/Q)/\pi$ and is in excellent agreement with Fig. 8. From a numerical point of view, this approximation is much less time consuming than the full resolution of Eq. (54). In fact, Eq. (54) required the integral over θ to be computed for each value of r (and at each iteration step) and the solving time was therefore n_r times larger than for Eq. (64).

Close to zero frequency, the density of states vanishes as $\rho_\varphi(\nu)\propto|\nu|$ since the density of eigenvalues $\rho(\lambda)$ is finite in $\lambda=0$, see Eq. (19). We now turn to negative, that is imaginary frequencies. Computing the integrated density of unstable modes, we see that the latter represents roughly 20% of acoustic modes. They extend down to frequencies equal to $\nu_- = -20$ cm^{-1} with a maximum in $\nu \simeq -3.5$ cm^{-1}. We shall come back to the physical implications of these modes in the next section.

The relation of dispersion $\nu_\varphi(q)$ for acoustic modes is displayed in Fig. 9 over the whole range of real and imaginary frequencies. We also show on Fig. 10 the inverse autocorrelation length $\sigma_\varphi(\nu)$. As for optical modes, the dispersion relations at $T=300$ K gets close to its zero temperature counterpart at intermediate wave numbers $0.5 \leqslant q \leqslant 1.5$ corresponding to frequencies 0 cm$^{-1} \leqslant \nu \leqslant 10$ cm^{-1}. This coincidence is accompanied by small values of σ on this interval of frequencies, giving rise to a coherence length of the order of $\xi \simeq 2$. Conversely, large frequencies correspond to highly disordered modes: $q \geqslant 2$ and monotonously increasing σ, with $\xi \simeq 0.4$ at $\nu=30$ cm^{-1}. Notice that the statical correlation length is the same as for optical modes, see Sec. V B.

Unstable modes have also short autocorrelation lengths, e.g., $\xi \simeq 0.4$ at $\nu=-20$ cm^{-1}. However, their wave numbers are much smaller and can be considered as constant (and zero) for $\nu \leqslant -10$. The autocorrelation function of unstable eigenmodes, Eq. (38), therefore does not change sign over a typical distance $d_s \sim \pi/q \gg 1$. Unstable modes can be seen as

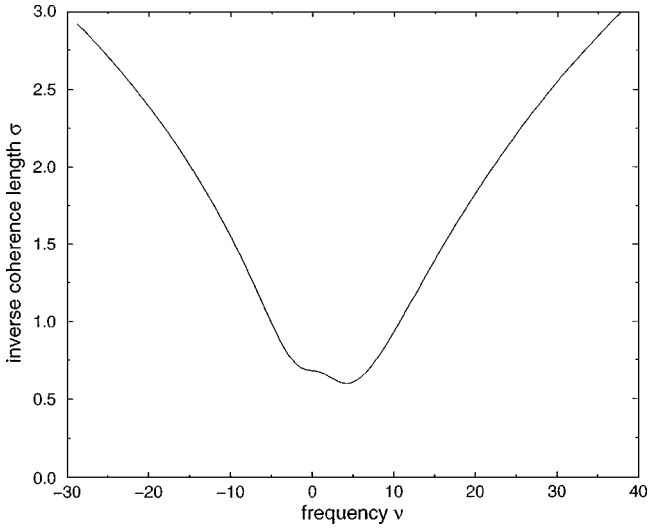

FIG. 10. Inverse coherence length $\sigma_\varphi(\nu)$ for acoustic modes. Negative frequencies represent unstable modes according to the convention exposed in Sec. III B. Note the inflection point at $\nu=0$ due to this representation, see Sec. V C.

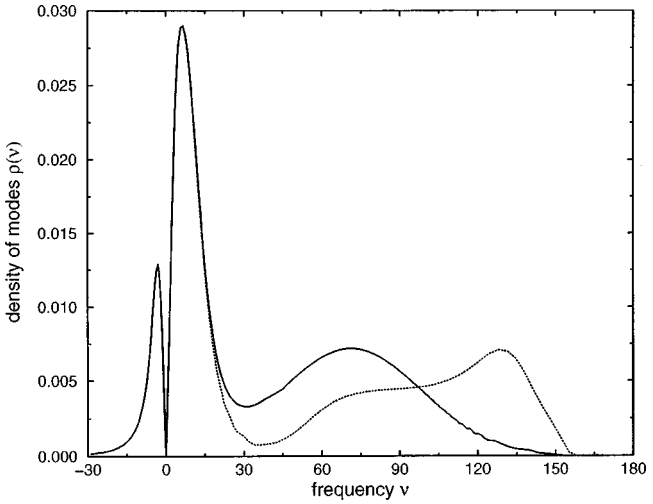

FIG. 11. Spectrum $\rho(\nu)$ for both optical and acoustic modes. Parameters are: $D=0.15$ eV, $E=0.74$ eV/Å^2 (full curve) and $D=0.16$ eV, $E=4$ eV/Å^2 (dotted curve). Each spectrum is normalized to unity.

unstable acoustic phonons, involving coherent rotations of the molecule extending over regions of size d_s.

To end with, notice that the dispersion relation and the inverse coherence length both exhibit an inflection point in $\nu=0$ as shown in Figs. 9 and 10. This is an artifact of the representation of unstable modes as negative frequencies. Consider for instance the damping width σ close to zero frequency. In the natural λ eigenvalue parametrization, we expect a nonsingular behavior in the vicinity of $\lambda=0$: $\sigma(\lambda)=\sigma_0+\sigma_1\lambda+O(\lambda^2)$. For positive eigenvalues λ, the frequency ν is defined as $\nu\propto\sqrt{\lambda}$, Eq. (19), while using the negative-imaginary convention of Sec. III B, $\nu\propto-\sqrt{-\lambda}$ for negative eigenvalues. The expansion of the inverse coherence length as a function of (small) frequencies thus reads $\sigma(\nu)=\sigma_0+\tilde{\sigma}_1\nu\cdot|\nu|+O(|\nu|^3)$ and is singular with an inflection point in $\nu=0$.

D. Origin of acoustic modes: Torsional and compressional vibrations

As we have seen in Sec. II A, the axial distance h_j between two successive base pairs is a function of the radii r_j, r_{j-1} and of the twist angle θ_j, see Eq. (2). To study the compressional and stretching modes of the helix, that is the fluctuations of the h_js, we therefore linearize Eq. (2) around the initial configuration $\mathcal{C}$ of the independent degrees of freedom r_j, φ_j. As a result, the fluctuations of the heights $\delta_j = z_j - z_j^{\mathcal{C}}$ appear to be linear combinations of the displacement variables y_j and ϕ_j introduced in Sec. III B,

$$\delta_j-\delta_{j-1}=A^{\mathcal{C}}_{1,j}y_j+A^{\mathcal{C}}_{2,j}y_{j-1}+B^{\mathcal{C}}_j(\phi_j-\phi_{j-1}), \qquad (65)$$

where the coefficients $A^{\mathcal{C}}_{1,j}$, $A^{\mathcal{C}}_{2,j}$, $B^{\mathcal{C}}_j$ depend on the initial configuration.

At low frequency, optical modes are irrelevant. So radial displacements y_j are null. On the opposite, acoustic modes are present and give rise to angular vibrations of the base pairs in the planes perpendicular to the molecular axis ($\phi_j \neq 0$). From Eq. (65), we see that the latter are accompanied by displacements of the pairs along this axis ($\delta_j \neq 0$). As a consequence, acoustic modes give rise to simultaneous torsional and compressional vibrations.

In principle, at higher frequencies, excitations of radial optical modes could take place and would also give rise to fluctuations of the distances between base pairs along the axis. However, such excitations would not correspond to the acoustic wave seen in experiments as discussed below.

E. Discussion

Our calculation shows that the coherence length of normal modes is finite and remains of the order of unity. Eigenvectors at finite temperature are thus far from being plane waves as in the zero temperature case. The power spectrum, that is the Fourier transform of the autocorrelation function at frequency ν, Eq. (47), acquires a Lorentzian form centered around a certain wave number $q(\nu)$ with a width $\sigma(\nu)$. This behavior is experimentally observed in neutron scattering experiments.[1,20] Furthermore, the calculation justifies *a posteriori* the absence of selection rule on momentum in Raman experiments. Indeed, the coherence length of the disordered phonons is of the order of $\xi H \leqslant 15$ Å and is negligible with respect to optical wavelengths $\simeq 4800$ Å, see Sec. III C.

Both optical and acoustic spectra are superposed in Fig. 11. The total spectrum $\rho(\nu)$ equals $\rho_r(\nu)+\rho_\varphi(\nu)$ is normalized to unity (half of modes originate from angular degree of freedom, and the remaining half from optical ones). The acoustic peak appears much more narrow and higher than its optical counterpart. The width of the latter amounts to $\Delta\nu \simeq 60$ cm^{-1} (respectively $\Delta\nu\simeq 100$ cm^{-1}) for $E=0.74$ eV/Å^2 (respectively for $E=4$ eV/Å^2) whereas (stable) acoustic modes spread over a range of $\Delta\nu\simeq 15$ cm^{-1}. While for $E=4$ eV/Å^2, acoustic and optical spectra do not intersect each other, there is an overlap region at smaller stiffness constant around $\nu\simeq 30$ cm^{-1}. Nevertheless, both fluctuations take place on basically two distinct time scales. Acoustic modes correspond to torsional and compressional vibrations

of the molecule and are associated to a typical frequency of $\simeq 10\ \mathrm{cm}^{-1}$, or equivalently to a typical time $\tau_v \simeq 3\ 10^{-12}$ s. Radial optical modes correspond to radial hydrogen bond fluctuations and are present at frequencies $\simeq 100\ \mathrm{cm}^{-1}$, that is, involve dynamical processes on a scale $\tau_r \simeq 0.3\ 10^{-12}$ s. At low frequencies $|\nu| < 25\ \mathrm{cm}^{-1}$, the presence of unstable modes threatens the validity of the linearization procedure used in Sec. III B. A more refined analysis taking into account nonlinear terms in the dynamical equations is needed to understand how unstable modes (with low wave numbers q) are coupled to stable mode (with larger q) and modify the frequencies of the latter. Conversely, the absence of unstable modes at frequencies larger than $\nu > 25\ \mathrm{cm}^{-1}$ indicate that the INM predictions are reliable for time scales smaller than 10^{-12} s. This is enough to identify the range of allowed frequencies for acoustic modes: $\nu < 30\ \mathrm{cm}^{-1}$. The INM prediction for the location of the acoustic peak $\nu_M \simeq 7\ \mathrm{cm}^{-1}$ cannot be trusted blindly but it reasonably lies in the middle of the zero temperature band, see Sec. III D.

We now turn to the comparison with spectroscopy measurements. To establish the link between the density of states and the Raman intensity, the knowledge of the light-to-vibrations coupling $C(\nu)$ is necessary as seen in Sec. III C. In the absence of precise information on the latter, we have rescaled the density of modes $\rho(\nu)$ according to formula (20) for the three different choices $C(\nu)=1$, $C(\nu)=\nu$, and $C(\nu)=\nu^2$ (note that the second hypothesis for C is the most plausible one). The resulting theoretical Raman intensities are shown in Fig. 12(a) for $E=0.74\ \mathrm{eV/\AA^2}$ and Figure 12(b) for $E=4\ \mathrm{eV/\AA^2}$. On the one hand, the overall shape of the spectra change with C with respect to ρ. In particular for $C(\nu)=1$ and $C(\nu)=\nu$, the acoustic peak diverges at small frequencies and the optical-modes bump acquires a shoulder form (for $E=0.74$), located in the right flank of the acoustic modes. On the other hand, the band of allowed optical frequencies remains unaltered by the choice of C and extends over $50 < \nu < 100\ \mathrm{cm}^{-1}$ for $E=0.74$ and $50 < \nu < 150\ \mathrm{cm}^{-1}$ for $E=4$. In the latter case, the optical region of the spectrum exhibit two local maxima at the same height for $C(\nu)=\nu$. The rescaled spectrum of Fig. 12(a) for $C(\nu)=\nu$ closely agrees with intensity curves obtained from Raman experiments at $T=50\ ^\circ\mathrm{C}$ and shown in Fig. 2 of Ref. 7 on the range of frequencies $50 < \nu < 100\ \mathrm{cm}^{-1}$. The latter measurement was performed on calf thymus in solution (10 mM PHB, pH=7). This allows us to think that $E=0.74$ is a better choice for the stiffness constant than $E=4$.[29]

Our results do not show drastic variations with temperature for T ranging from 300 K to the melting temperature $T_m = 350$ K. At T_m the double helix structure disappears and so do all helix-related modes. Since denaturation is described as a first-order phase transition by the present model, there is no gradual destabilization of the modes and no relevant change in ρ can be seen as mentioned above. The experimental Raman measurements shown on Fig. 2 of Ref. 7 nevertheless show a smooth change in the shape of the intensity curves over the temperature interval $50\ ^\circ\mathrm{C} < T < 80\ ^\circ\mathrm{C}$. This apparent paradox can be easily explained by the fact that our model describes a homogeneous sequence of bases. For the latter, the fraction of open base pairs vs. temperature exhibits

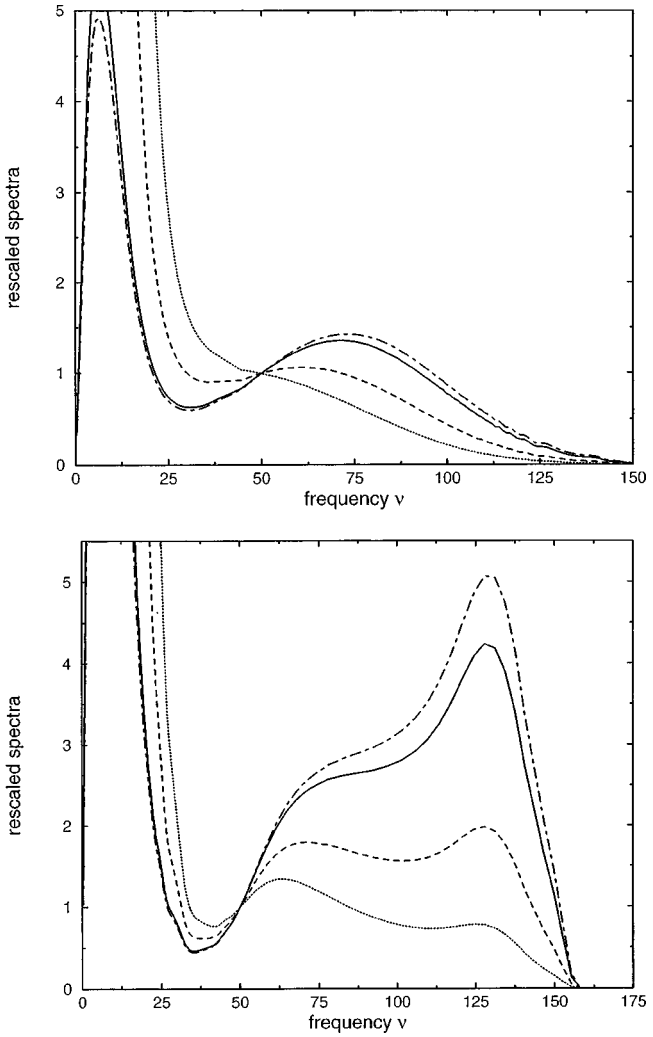

FIG. 12. Rescaled spectra for different light-to-vibrations coupling C for parameters $D=0.15$ eV, $E=0.74\ \mathrm{eV/\AA^2}$ (a) and $D=0.16$ eV, $E=4\ \mathrm{eV/\AA^2}$ (b). Original spectra $\rho(\nu)$ are recalled (full lines) and rescaling functions are: $C(\nu)=1$ (dotted curve), $C(\nu)=\nu$ (dashed curve), and $C(\nu)=\nu^2$ (dashed-dotted curve). Vertical units are arbitrary, all curves have been multiplied by a constant to meet (and equal unity) in $\nu=50\ \mathrm{cm}^{-1}$.

an abrupt jump from zero to one at T_m.[42] In the case of a heterogeneous sequence as in the experiments of Ref. 7, the denaturation temperature of AT rich regions can be inferred to be $T_m = 50\ ^\circ\mathrm{C}$,[42] and the fraction of open base pairs smoothly increases from zero to one over the range of temperatures $50\ ^\circ\mathrm{C} < T < 77\ ^\circ\mathrm{C}$.

We now turn to acoustic modes. Raman measurements on fibers at 100% of relative humidity (rh) have given evidence for a narrow band at $16\ \mathrm{cm}^{-1}$, see Fig. 1 of Ref. 9. This peak shifts down to lower frequencies ($10\ \mathrm{cm}^{-1}$) when increasing the hydration degree of DNA in gels and disappears in the central component for DNA in solution.[7] Other measurements on B-DNA fibers at lower $\simeq 80\%$ rh by Lindsay *et al.* have reported a similar band at a higher frequency $\nu \simeq 25\ \mathrm{cm}^{-1}$ that shifts to lower values as the rh increases in good agreement with Urabe *et al.*'s data.[10] The observed softening of the frequency may come from the weakening of external, e.g., interhelical interactions as well as from the

influence of the (rigid) primary and (viscous) secondary water shells, see Sec. III A. Note that these modes seem to appear when the scattering vector $\Delta\vec{Q}$ gets parallel to the helical axis. Other molecular systems as crystals of ATP (that do not include hydrogen bond interactions) or guanosine self-associates (without phosphate) that present a columnar stacking of bases exhibit similar low frequency spectra. The intensity of the low frequency (<20 cm^{-1}) mode was found to depend mostly on the stacking degree of bases in a column.[11] Our calculation predicts, despite the presence of unstable INM that acoustic modes are predominant for $\nu < 25$ cm^{-1}. The statement by Urabe *et al.* that low frequency modes ($\nu < 25$ cm^{-1}) are related to vibrations of the base pairs column[9,11] is in full agreement with our theoretical analysis. In addition, the calculated range of frequencies as well as the acoustic nature of the modes (see Fig. 9) are in good agreement with the compressional modes observed in neutron scattering experiments.[1]

A quantitative comparison of our dispersion relations for acoustic modes with experimental results is difficult due to the lack of available data. Neutron scattering measurements have shown that pseudodispersion relations with a finite damping width can be obtained for low frequencies but these experiments have been performed on crystalline DNA fibers. Our model (and the values of parameters exposed in Sec. II C) are valid for DNA in solution where the interaction with surrounding water is radically different and interhelical effects are absent. More precisely, we find that at fixed momentum q, the experimental frequency ν for fibers is larger than the theoretical predictions for diluted DNA. The additional mass due to primary water shells for DNA in solution may account for the reduction of frequency to a large extent.[10] Conversely, the extrapolated value of σ is constant and equal to 0.48 in good agreement with the theoretical minimum $\sigma = 0.5$ shown in Fig. 10.

VI. SUMMARY AND CONCLUSION

In this article, we have shown how to apply the INM framework to a simple model of DNA molecule and reproduce the main features of collective vibration modes at finite temperature. Time scale separation between atomic bond vibrations and collective modes allows to obtain good results at low frequencies without resorting to a detailed description of DNA at the atomic level. This simplified modelization of DNA permits in turn a deeper analytical understanding of the structure of the modes than, e.g., within MSPA.

The model we had introduced to reproduce thermally- and mechanically-induced DNA denaturation transitions has proven to be also capable of describing accurately the picosecond dynamics seen through spectroscopy measurements. The reason is that, in spite of its simplicity, this model provides a sensible description of the helical structure of DNA and is able to reproduce the couplings between radial expansion, torsional motion, and axial compression. This result has been obtained without any modification of the model or any new fit of the constant force or geometrical parameters. Remarkably, the comparison with Raman experiments has permitted us to decide the value of the only parameter known with some uncertainty from the denaturation experiments, that is, the stacking stiffness E. The success of the present model to account for completely different experiments comes from its mesoscopic nature that lies at an intermediate level between microscopic modelizations, e.g., studies by Prohofsky *et al.*[12] or numerical simulations by Lavery and collaborators,[51] and elasticity theories as the worm-like-chain model[52] and its recent extensions.[53]

Our calculation gives access to the density of modes $\rho(\nu)$ and some statistical properties of the normal modes as the dispersion relation $\nu(q)$ and the autocorrelation length $1/\sigma(\nu)$. The dispersion relations provide the power spectrum of the modes which exhibit a finite damping width σ at ambient temperature.

Let us summarize briefly our main quantitative result. Through a rescaling of the density of modes taking into account the light-to-vibrations coupling C, we have related the density of modes to Raman intensity measurements. The range of frequencies corresponding to optical, i.e., base pair stretching modes do not qualitatively depend on C. The choice of parameters $D = 0.15$ eV, $E = 0.74$ eV/Å^2 gives, in good agreement with the experiments by Urabe *et al.* [see Fig. 12(a) and Fig. 2 in Ref. 7], 50 cm$^{-1} < \nu < 100$ cm^{-1}. Furthermore, this range remains roughly unchanged in the whole interval of temperatures $0\,°\text{C} < T < T_m$ where $T_m = 77\,°\text{C}$ is the denaturation temperature. Indeed, our model describes a homogeneous sequence for which the melting transition is very abrupt and not smooth as for disordered DNA. Furthermore, the good agreement of our results with experimental data suggests that neglecting viscous damping terms in the equations of motion is a reliable approximation for hydrogen bonds stretching modes. This is corroborated by the very small amplitude of the motion inside the hydrogen bond well ($\simeq 0.1-0.2$ Å) that should not induce rearrangements of surrounding water molecules responsible for viscosity.

It would be very interesting to compare our theoretical results for $\sigma_r(\nu)$ and $\nu_r(q)$ with neutron scattering experiments which to our knowledge are not available for DNA in solution over the range of frequencies mentioned above. A fundamental feature of the modes is that the coherence length ξ is of the order of unity: decorrelation between components of the same mode takes place on a few angstroms. This prediction agrees well with results for the static correlation distance ζ obtained from statistical mechanics calculations as seen in Sec. V B.

As for acoustic modes that correspond to torsional and compressional vibrations, the predicted characteristic frequencies $\nu < 25$ cm^{-1} coincide with Raman measurements $\nu < 16$ cm^{-1}, see Ref. 11. The value of the coherence length in the center of the spectrum, $\xi = 1/\sigma \simeq 6.8$ Å is compatible with data obtained through neutron scattering experiments on DNA fibers.[1] However, as far as acoustic modes are concerned, the present approach suffers from two weaknesses. First, we have not taken into account in the dynamical equa-

tions the viscous forces that might be relevant. Second, INM can become unstable at small ν and the linearization approximation we have used throughout the study becomes dangerous. Further information about the nonlinear couplings between modes would be extremely useful to circumvent this difficulty. It is however not clear how such a study could be technically pursued.

ACKNOWLEDGMENTS

We are particularly grateful to W. Baumruk and P. Y. Turpin for motivating and enlightening discussions on the experimental aspects of this work. We also thank J. F. Leger, L. Bourdieu, A. Colosimo, D. Chatenay, M. Peyrard, and H. Urabe for advice and discussions.

APPENDIX: VARIATIONAL CALCULATION AND SELF-CONSISTENT EQUATION FOR Q

In this appendix, we compute the Rayleigh–Ritz functional for both the ground state, Eq. (53) and the first excited Eq. (57) (with $l=1$) wave functions. We then derive the saddle-points equations on the variance $Q(r)$ for both instantaneous modes families.

1. Calculation of the ground state

Inserting the Gaussian ansatz, Eq. (53) in (50), we obtain

$$\mathcal{R}[\Psi_0^g]=\frac{\displaystyle\int_{r_{\min}}^{\infty} dr\ dr' \int_0^{\pi} d\theta\ T(r,r',\theta)\psi_0(r)\psi_0(r')\ \{\mathcal{W}(r,r',\theta)\}^{-n/2}}{\displaystyle\int_{r_{\min}}^{\infty} dr\,\psi_0(r)^2\ \{-8\pi i Q(r)\}^{-n/2}}$$

$$=\lambda_0+\frac{n}{2}\ r^g[Q]+O(n^2), \tag{A1}$$

where $\mathcal{W}$ [Eq. (55)] is the determinant of the two by two matrix $\mathcal{M}$ defined by

$$\mathcal{M}=\begin{pmatrix} Q(r)+\lambda+i\epsilon-d_0(r,r',\theta) & d_1(r,r',\theta) \\ d_1(r,r',\theta) & Q(r')+\lambda+i\epsilon-d_0(r',r,-\theta)\end{pmatrix}, \tag{A2}$$

and

$$r^g[Q]=\lambda_0\ \int_{r_{\min}}^{\infty} dr\psi_0(r)^2\ln Q(r)-\int_{r_{\min}}^{\infty} dr dr' \int_0^{\pi} d\theta\ T(r,r',\theta)\psi_0(r)\psi_0(r')\ln\mathcal{W}(r,r',\theta), \tag{A3}$$

up to an irrelevant additional constant. The vanishing condition (52) on the functional derivative of $r^g[Q]$ with respect to $Q(r)$ leads to Eq. (54).

2. Calculation of the first excited state

We now compute Λ_1^g using ansatz (57) and expression (50). The denominator of $\mathcal{R}[\Psi_1^g]$ reads

$$\langle\Psi_1^g|\Psi_1^g\rangle=\int_{r_{\min}}^{\infty} dr \int_{-\infty}^{\infty} d\varphi \int d\vec{x}\ \psi_0(r)^2\ x_1^2\ \exp\left(\frac{i}{2}Q(r)\ \vec{x}^2\right)$$

$$=i\ \ C\ \ \int_{r_{\min}}^{\infty} dr\ \psi_0(r)^2\ Q(r)^{-1}, \tag{A4}$$

when $n\to 0$. $C=\int_{-\infty}^{\infty} d\varphi$ could be made finite by limiting the range of the twist angle. Such a regularization is however not necessary since C also appears in the numerator of Eq. (50),

$$\langle\Psi_1^g|\mathcal{T}|\Psi_1^g\rangle=\int_{r_{\min}}^{\infty} dr\,dr' \int_{-\infty}^{\infty} d\varphi\, d\varphi'\ T(r,r',\varphi-\varphi')\ \psi_0(r)\ \psi_0(r') \int d\vec{x}\ d\vec{x}'\ x_1 x_1'\ \exp\left[\frac{i}{4}\begin{pmatrix}\vec{x}\\ \vec{x}'\end{pmatrix}^{\dagger}.\mathcal{M}.\begin{pmatrix}\vec{x}\\ \vec{x}'\end{pmatrix}\right]$$

$$=2\ i\ C\ \ \int_{r_{\min}}^{\infty} dr\ dr' \int_0^{\pi} d\theta\ T(r,r',\theta)\ \psi_0(r)\ \psi_0(r')\ (\mathcal{M}^{-1})_{12}(r,r',\theta), \tag{A5}$$

as the number of replicas n vanishes. Using $\Lambda_0^g\to\lambda_0$ when $n\to 0$, we obtain Eq. (58).

3. Self-consistent equation for the radius Hessian matrix

For base pair vibrations, the second derivatives d_0 and d_1 are given in Eq. (32) and do not depend on the relative twist θ between successive base pairs. Inserting Eq. (32) into the extremization Eq. (54) for $Q(r)$ and using the definition, Eq. (11) of the effective radial transfer matrix T_0, we obtain

$$\frac{\lambda_0 \psi_0(r)}{2Q(r)} = \int_{r_{\min}}^{\infty} dr'\, T_0(r,r')\, \psi_0(r') \;\; \frac{Q(r')+\lambda+i\epsilon-\frac{1}{2}V_m''(r')-2E}{\mathcal{W}_r(r,r')}, \tag{A6}$$

where

$$\mathcal{W}_r(r,r') = \left(Q(r)+\lambda+i\epsilon-\tfrac{1}{2}V_m''(r)-2E\right)\left(Q(r')+\lambda+i\epsilon-\tfrac{1}{2}V_m''(r')-2E\right)-4E^2. \tag{A7}$$

The ratio Eq. (58) of the first two eigenvalues of $\mathcal{T}$ is given by

$$\frac{\Lambda_1^g}{\Lambda_0^g} = -4E\left\{\int_{r_{\min}}^{\infty} dr\; dr'\;\; \frac{T_0(r,r')}{\mathcal{W}_r(r,r')}\, \psi_0(r)\; \psi_0(r')\right\} \Bigg/ \left\{\lambda_0 \int_{r_{\min}}^{\infty} dr\; \psi_0(r)^2 Q(r)^{-1}\right\}. \tag{A8}$$

4. Self-consistent equation for the angular Hessian matrix

For angular fluctuations, the elements d_0, d_1 of the matrix $\mathcal{D}_{\varphi}^{\mathcal{C}}$ of second derivatives depend on radii r, r' as well as on the angle θ. No simplification arises as in the base pairs case. The saddle-point equation for $Q(r)$ is precisely Eq. (54) but care must be paid to the backbone potential $V_b(r,r',\theta)$. As can be seen from definition (6), the angular integral in Eq. (54) is restricted to twist angles θ fulfilling the condition

$$\cos\theta > \frac{r^2+r'^2-L^2}{2rr'}. \tag{A9}$$

Indeed, when the inequality in Eq. (A9) is not satisfied, the potential V_b is infinite, see discussion of Sec. II A. The same prescription holds for the angular integral in Eq. (58).

[1] H. Grimm, H. Stiller, C. F. Majkrazak, A. Rupprecht, and U. Dahlborg, Phys. Rev. Lett. **59**, 1780 (1987).
[2] H. Grimm and A. Rupprecht, Physica B **174**, 291 (1991).
[3] H. Grimm and A. Rupprecht, Physica B **234–236**, 183 (1997).
[4] J. F. Marko and B. M. Pettitt, *Fluctuations of DNA Double Helix Structure*, preprint.
[5] D. P. Millar, R. J. Robbins, and A. H. Zewail, J. Chem. Phys. **76**, 2080 (1982).
[6] P. Painter, L. Mosher, and C. Rhoads, Biopolymers **20**, 243 (1981).
[7] H. Urabe and Y. Tominaga, J. Phys. Soc. Jpn. **50**, 3543 (1981).
[8] H. Urabe, Y. Tominaga, and K. Kubota, J. Chem. Phys. **78**, 5937 (1983).
[9] H. Urabe, H. Hayashi, Y. Tominaga, Y. Nishimura, K. Kubota, and M. Tsuboi, J. Chem. Phys. **82**, 531 (1985).
[10] S. M. Lindsay, S. A. Lee, J. W. Powell, T. Weidlich, C. Demarco, G. D. Lewen, N. J. Tao, and A. Rupprecht, Biopolymers **27**, 1015 (1988).
[11] H. Urabe, Y. Sugawara, M. Tsukakoshi, and T. Kasuya, J. Chem. Phys. **95**, 5519 (1991).
[12] E. W. Prohofsky, *Statistical Mechanics and Stability of Macromolecules* (Cambridge University Press, Cambridge, 1995).
[13] J. M. Eyster and E. W. Prohofsky, Biopolymers **13**, 2505 (1974); **13**, 2527 (1974).
[14] Y. Gao, K. V. Devi-Prasad, and E. W. Prohofsky, J. Chem. Phys. **80**, 6291 (1984).
[15] Y. Z. Chen and E. W. Prohofsky, Phys. Rev. E **49**, 873 (1993).
[16] Y. Z. Chen and E. W. Prohofsky, Phys. Rev. E **49**, 3444 (1993).
[17] Y. Z. Chen, Y. Zhang, and E. W. Prohofsky, Phys. Rev. E **55**, 5843 (1997).
[18] V. Lisy, P. Miskovsky, and P. Schreiber, J. Biomol. Struct. Dyn. **13**, 707 (1996).
[19] C. Kittel, *Introduction to Solid State Physics* (Wiley, New York, 1986).
[20] V. V. Prabhu, W. K. Schroll, L. L. Van Zandt, and E. W. Prohofsky, Phys. Rev. Lett. **60**, 1587 (1988); H. Grimm and H. Stiller, *ibid.* **60**, 1588 (1988).
[21] R. Shuker and R. Gammon, Phys. Rev. Lett. **25**, 222 (1970).
[22] A. J. Martin and W. Brenig, Phys. Status Solidi B **64**, 163 (1974).
[23] B. Souillard, ''*Waves and Electrons in Random Media,*'' Chance and Matter, Les Houches session XLVI (Elsevier, New York, 1986).
[24] S. R. Elliott, *Physics of Amorphous Materials* (Longman Scientific and Technical, London, 1990).
[25] T. Keyes, J. Phys. Chem. A **101**, 2921 (1997).
[26] Y. Wan and R. Stratt, J. Chem. Phys. **100**, 5123 (1994).
[27] G. Biroli and R. Monasson, J. Phys. A **32**, L255 (1999).
[28] A. Cavagna, I. Giardina, and G. Parisi, Phys. Rev. Lett. **83**, 108 (1999).
[29] S. Cocco and R. Monasson, Phys. Rev. Lett. **83**, 5178 (1999).
[30] S. B. Smith, L. Finzi, and C. Bustamante, Science **258**, 1122 (1992).
[31] R. H. Austin, J. P. Brody, E. C. Cox, T. Duke, and W. Volkmuth, Phys. Today **32** (1997) and references therein.
[32] T. R. Strick, J.-F. Allemand, D. Bensimon, A. Bensimon, and V. Croquette, Science **271**, 1835 (1996).
[33] T. R. Strick, J.-F. Allemand, D. Bensimon, R. Lavery, and V. Croquette, Physica A **263**, 392 (1999).
[34] R. Monasson, Eur. Phys. J. B **12**, 555 (1999).
[35] D. J. Thouless, Phys. Rep., Phys. Lett. **13**, 93 (1974); *Mesoscopic Quantum Physics*, Les Houches session LXI (Elsevier, New York, 1995).
[36] M. Barbi, S. Cocco, and M. Peyrard, Phys. Lett. A **253**, 358 (1999).
[37] Vibrations of the sugar puckering modes that could be in the frequency range of interest will not be considered here.
[38] M. Peyrard and A. R. Bishop, Phys. Rev. Lett. **62**, 2755 (1989).
[39] T. Dauxois and M. Peyrard, Phys. Rev. E **51**, 4027 (1995).
[40] J. A. McCammon and S. C. Harvery, *Dynamic of Proteins and Nucleic Acids* (Cambridge University Press, Cambridge, 1987).
[41] Y. Zang, W. Zheng, J. Liu, and Y. Z. Chen, Phys. Rev. E **56**, 7100 (1997).
[42] W. Saenger, *Principles of Nucleic Acid Structure* (Springer-Verlag, New York, 1984); C. R. Calladine and H. R. Drew, *Understanding DNA* (Academic, San Diego, 1997).
[43] G. Parisi, *Statistical Field Theory* (Addison-Wesley, Redwood City, CA, 1988).
[44] H. Urabe, Y. Sugawara, M. Ataka, and A. Rupprecht, Biophys. J. **74**, 1533 (1998).
[45] S. N. Volkov and A. M. Kosevich, J. Biomol. Struct. Dyn. **8**, 1069 (1991).
[46] Y. Tominaga, K. Kubota, H. Urabe, Y. Nishimura, and M. Tsuboi, J. Chem. Phys. **83**, 5972 (1985).
[47] V. K. Malinovsky, V. N. Novikov, P. P. Parshin, A. P. Sokolov, and M. G. Zemlyanov, Europhys. Lett. **11**, 43 (1990).
[48] A. P. Sokolov, A. Kisliuk, D. Quitmann, and E. Duval, Phys. Rev. B **48**, 7692 (1993).
[49] J. M. Luck, *Systèmes Désordonnés Unidimensionels* (Aléa Saclay, 1992).
[50] S. Cocco and R. Monasson (unpublished).
[51] A. Leburn and R. Lavery, J. Biomol. Struct. Dyn. **16**, 593 (1998).
[52] J. F. Marko and E. Siggia, Science **265**, 506 (1994).
[53] C. Bouchiat and M. Mézard, Phys. Rev. Lett. **80**, 1556 (1997).